NBSIR 83-2731

Vaporization of Simulated Nuclear Waste Glass

U.S. DEPARTMENT OF COMMERCE
National Bureau of Standards
Center for Materials Science
High Temperature Processes Group
Inorganic Materials Division
Washington, DC 20234

June 1983

Interim Report

U.S. DEPARTMENT OF COMMERCE
NATIONAL BUREAU OF STANDARDS

NBSIR 83-2731

VAPORIZATION OF SIMULATED NUCLEAR WASTE GLASS

J. W. Hastie, E. R. Plante, and D. W. Bonnell

U.S. DEPARTMENT OF COMMERCE
National Bureau of Standards
Center for Materials Science
High Temperature Processes Group
Inorganic Materials Division
Washington, DC 20234

June 1983

Interim Report

U.S. DEPARTMENT OF COMMERCE, Malcolm Baldrige, *Secretary*
NATIONAL BUREAU OF STANDARDS, Ernest Ambler, *Director*

Table of Contents[a]

---

[a]In the interests of accuracy and clarity in describing various items of equipment or apparatus, mention has been made of commercial sources or brand names. This in no way implies endorsement of such products by the U.S. Government.

Vaporization of Simulated Nuclear Waste Glass

J. W. Hastie, E. R. Plante, and D. W. Bonnell
Center for Materials Science
National Bureau of Standards
Washington, DC 20234

ABSTRACT

Industrial development of nuclear waste glass processing requires basic data on glass vaporization thermodynamics. Detailed mass spectrometric experiments and thermodynamic estimates have been made for vaporization of a nonradioactive borosilicate glass containing representative nuclear waste isotopes. Alkali metaborates were observed to be the dominant vapor species and their partial pressures indicate significant vapor transport under likely process conditions. The results indicate the following order of significance for vapor transport of radionuclide species, Cs ~ Re (~ Tc) > Ru >> Sr.

Key words: Glass, mass spectrometry, nuclear waste, thermodynamics, vaporization.

1. Introduction

Industrial plans for nuclear waste storage require the waste to be incorporated into a borosilicate glass. Vapor pressure data are needed for these borate-waste forms in order to optimize the process conditions (e.g., temperature, composition) and minimize losses of radionuclides

by vapor transport during the high temperature mixing treatment. The primary objective of the present study was to define the vaporization thermodynamics of a simulated nuclear waste (SNW) borosilicate glass, containing non-radioactive isotopes, as prepared by DuPont-Savannah River. Also, measurements of partial pressure for each vapor species allow thermodynamic activities and related partial molar functions to be derived. Such basic data are pertinent to the development of thermodynamic models of other nuclear waste properties such as leaching and storage durability. Special emphasis was given to vapor species containing the following elements which in actual nuclear waste form are highly radioactive: Cs, Sr, Ru, and Re--present as a technetium simulant.

Table 1 gives the analytical and nominal compositions of the glass sample used. The analytical composition was determined by inductively coupled plasma spectroscopic analysis [Soper, 1982] for all elements except Cs, Ru, and Re which were determined by neutron activation analysis. For the thermodynamic estimation of species pressures the nominal glass composition data were used.

No literature data exist for a glass of this type. However, there are indications from vapor transport measurements on metaborate glasses, both in inert and H_2O atmospheres, that alkali metaborate and metaboric acid are the likely vapor species [Cable, 1978; Wenzel and Sanders, 1982]. The thermogravimetric data of Gray [1980] for radioactive waste glasses, with higher concentrations of radionuclides than for the present system, is not molecular-specific and hence cannot be used for extrapolation to our conditions.

High temperature vaporization data were required for vacuum, inert N_2, and reactive H_2O, CO_2, CO, H_2, O_2 atmospheres, the latter mixture

Table 1

Simulated Nuclear Waste (SNW) Glass Composition[a]

Compound	Nominal Composition Weight %	Nominal Composition Mole %	Analytical Composition[b] Weight %	Analytical Composition[b] Mole %
SiO_2	52.00	57.01	53.76	59.40
Fe_2O_3	12.96	5.35	11.49	4.78
Al_2O_3	4.86	3.14	4.75	3.09
B_2O_3	7.29	6.70	6.49	6.19
Li_2O	5.10	11.25	3.96	8.80
Na_2O	10.13	10.76	8.59	9.20
MnO_2	3.25	1.36	3.57	2.72
NiO	1.05	0.93	1.80	1.60
CaO	1.59	1.87	1.01	1.19
MgO	0.68	1.11	0.54	0.88
ZrO_2	0.70	0.38	3.79	2.04
SrO	0.09	0.06	0.05	0.03
Cs_2O	0.10	0.03	0.07	0.02
RuO_2	0.09	0.05	0.11	0.05
Re_2O_7	0.10	0.01	0.03	0.01

[a] [Soper, 1982]

[b] See text for selection

representing the off-gas condition in the industrial glass processor. For the temperature range of interest, 850 to 1150 °C, this glass is in a molten state. Under the conditions of interest we can expect a priori an exceedingly complex vapor phase composition--containing many types of polyatomic species--and measurements over a wide dynamic range of pressure and temperature are required for an unambiguous thermodynamic analysis. Specialized state-of-the-art mass spectrometric techniques are required to characterize such complex systems. Three techniques, Knudsen effusion Mass Spectrometry (KMS), Gas Inlet KMS (GKMS), and Transpiration Mass Spectrometry (TMS) were selected for the present study. These techniques were supplemented by thermodynamic calculations which are at present approximate owing to assumptions concerning solution activities.

The experimental and theoretical results indicate that complex oxide vapor species dominate the vaporization behavior of this glass, with the following order of significance for the radionuclides

$$Cs \sim Re\ (\sim Tc) > Ru >> Sr.$$

Also, significant losses of the host glass components Li_2O, Na_2O, and B_2O_3 occur due to the high volatility of alkali metaborate species. Our experiments and thermochemical calculations suggest the reactive atmosphere to be of secondary importance, though additional experiments and detailed modeling are required for a definitive picture to emerge.

2. Knudsen Effusion Mass Spectrometry

2.1 Basis of Technique

Knudsen effusion mass spectrometry (KMS) combines the classical Knudsen method for vapor pressure measurement with mass spectrometric identification of individual molecular species. The rate of effusion is related to the pressure within the effusion cell by the expression:

$$\frac{m_i}{\Delta t} = P_i \cdot C \cdot a \, (2\pi RT/M_i)^{-\frac{1}{2}} \qquad (2.1)$$

where, for species i, m_i is the mass loss for time Δt, P_i the partial pressure, C the Clausing factor, a the orifice area, R the gas constant, T the temperature, and M_i the molecular weight. The partial pressure is determined from the mass spectrometric positive ion intensity I_i using the expression:

$$P_i = kI_iT, \qquad (2.2)$$

where k is the combined mass spectrometer-chemical species sensitivity constant.

These relationships are based on the condition of molecular effusion where the molecular mean free path within the cell is much larger than the orifice diameter. For practical orifice sizes of $\sim$ 0.5 mm and typical temperatures and molecular weights, the upper limit in cell pressure is about 10^{-4} atm for molecular effusion.

2.2 Apparatus

A schematic of the apparatus used is given in figure 1. Details of this apparatus have been given elsewhere [Plante, 1979]. To discriminate against scattered gas in the mass spectrometer ion source, beam modulation was used. In this method of operation, molecules issuing from the effusion orifice are interrupted at a selected frequency (about 200 Hz) by a slotted disc mounted on a motor. A light beam passing through the disc, and detected by an optical switch, serves as the reference signal for a lock-in amplifier. The mass-analyzed positive ions, formed by electron impact in the source of the mass spectrometer, are amplified by the lock-in detector only if they bear a specific and definite fixed phase relationship to the reference signal. This signal, which is called an ac spectrum, is relatively free from interference at the same m/e ratio from other ions which are formed in the source of the mass spectrometer but have not passed through the chopping wheel.

The quadrupole mass filter (QMF) shown in figure 1 is mounted about 1-1/2 inches off center on a 6-inch flange in a horizontal position. The water-cooled motor (M) which drives the modulation disk (MD) and the optical switch (OS) are located below the mass filter. The location of ion gauges (I.G.), and a shutter (S) for protecting the window (W) are also indicated. A prism (P) on the top flange deflects the radiant energy emitted from the Knudsen cell into an optical pyrometer for temperature measurement. However, for the relatively low temperatures of the present study a thermocouple (T.C.) was used for temperature measurement.

Figure 2 shows a schematic diagram of a typical Knudsen cell and furnace. The Knudsen cell was centrally located, both axially and

vertically, in the furnace. This arrangement was contained within a water-cooled copper chamber to reduce outgassing effects at elevated temperatures. The Knudsen cell was made of 0.025 cm Pt sheet and was of welded construction. It was 0.80 cm o.d. by 1.90 cm high and was welded to a 0.32 cm o.d. platinum mounting tube about 2.5 cm long. The top of the cell was made from 0.015 cm Pt sheet, the outer edge of which was bent in a mold to form a lip so that the lid fits snugly inside the effusion cell body (note detail in fig. 2). An effusion orifice diameter of 0.5 cm was used. For the present study, the cell was modified to include a reentrant thermocouple support tube located in the sample region (not shown in fig. 2).

For measurements involving injection of water vapor through the cell bottom, the Knudsen cell was modified by insertion of a Pt leak tube connected to a gas inlet system. A 0.025 cm (0.010 in.) orifice at the top of the leak tube allowed for water vapor injection into the cell. The leak rate into the cell was controlled by a valve external to the vacuum system. With this cell arrangement, temperatures were measured using a thermocouple spot welded to the side of the effusion cell.

The Ta sheet furnace, as shown in figure 2, was 7.6 cm long and 0.005 cm thick, with heavier gauge support rings connected to electrodes. High amperage low voltage power was supplied to this radiation furnace through water-cooled electrodes.

2.3 Instrument Calibration

2.3.1 Mass Discrimination

The quadrupole mass spectrometer may discriminate against higher mass ions, depending on tuning, and a mass discrimination calibration is necessary. For species i in a gas mixture, the ion current is given by the equation:

$$I_i^+ = k_g \cdot f_i \cdot \sigma_i \cdot A_i \cdot \tau_i \qquad (2.3)$$

where f_i is the fraction of species i in a gas mixture, A_i the isotopic fraction, σ_i the electron impact ionization cross section, τ_i the mass spectrometer transmission factor, and k_g the instrument geometric factor. Each term in equation (2.3) is known except the transmission and geometric factors, the latter being independent of ion type. Relative transmission factors were obtained from equation (2.3) using a gas mixture consisting of about 95% N_2 and 1% each of He, Ar, Ne, Kr, and Xe.

2.3.2 Sensitivity Constant

Two approaches are used to determine the sensitivity constant k_i defined in equation (2.2). These approaches rely either on a determination of the ion current corresponding to the evaporation of a known mass of material, or of the ion current corresponding to a known pressure in the effusion cell.

To determine the calibration constant by a mass calibration method the pressures from equations (2.1) and (2.2) are equated, giving

the relationship:

$$k_i = [m_i A_i (2\pi R)^{1/2}]/[Cat\ I_i^+ (M_i T)^{1/2}]. \qquad (2.4)$$

In practice, the sum of weight losses for a number of experiments at different temperatures and for different periods of time (Δt) are observed so that eq. (2.4) is cast in the form,

$$k_i = [A_i (2\pi R)^{\frac{1}{2}} \sum_T m_i]/[aC\ M_i^{\frac{1}{2}} \sum_T I^+ \Delta t \cdot T^{\frac{1}{2}}]. \qquad (2.5)$$

In some instances more than a single vapor species, or more than two vapor species linked by a known stoichiometric requirement, are formed. In such a case (which includes the simulated nuclear glass vaporization measurements) it is necessary to use measured or estimated ionization cross sections to relate the various sensitivity constants. In this case, the total mass loss ($\sum_i m_i$) can be used to estimate the various mass spectrometer constants for individual ions. Rearrangement of equation (2.5) for an individual species, i, gives:

$$\Delta m = k_g \cdot C \cdot a (2\pi R)^{\frac{1}{2}} \sum_i \frac{(M_i)^{\frac{1}{2}}}{A_i \tau_i \sigma_i} \left(\sum_T I_i(T) \cdot \Delta t(T) \cdot T^{\frac{1}{2}} \right). \qquad (2.6)$$

Using this equation, it is possible to calculate the contribution of each vapor species to the total estimated or measured weight loss and, thereby, determine if the estimated or measured cross sections are consistent with the sample stoichiometry.

Calibration of the mass spectrometer by passing a known amount of calibrating gas through a leak system is in principle the same as the weight loss method. For measurements where water vapor from an external source was passed over the glass using the KMS system

this calibration was obtained by passing Ar from a calibrated leak into the gas inlet tube of the Knudsen cell. Since the Ar leak rate is known (1.61×10^{-6} $cm^3 s^{-1}$), the equivalent pressure in the Knudsen cell can be calculated and a value of k_{Ar} determined from the Ar ion intensity. Values of k_i can then be calculated from k_{Ar} using equation (2.3).

For the various calibration and normal experimental procedures a 30 eV ionizing electron energy was used. The production of doubly ionized species for the calibration gases is minimal at 30 eV and the total ionization cross sections are a good approximation to the cross section for single ionization. Also, for more complex molecular species, the amount of fragmentation is less at 30 eV than at higher ionizing energies. In the case of electron impact fragmentation of molecular species it was necessary to either correct the estimated total cross section for this effect or to include in I_i all ions formed by fragmentation of a parent molecule. In this work, we have chosen to correct the total estimated cross section to obtain a partial ionization cross section valid for the observed species.

2.4 Detection Limits

The ability of the modulated beam mass spectrometer to detect different species depends on a number of factors. For mass positions relatively free of hydrocarbon or permanent gas background, such as at 23 amu, a signal of 1 μV can be detected with an uncertainty of ± 20%. For unfavorable mass positions, such as at 18 and 44 amu, signals of up to 5 μV may be required for detection within ± 20% uncertainty. Although it is possible to obtain greater total amplification by increasing the multiplier gain, the signal-to-noise ratio is a more important factor.

Improvement in this factor is usually achieved by decreasing the residual gas pressure in the mass spectrometer section of the vacuum system. Other factors of importance include, the distribution of isotopes among the nuclides, the instrument mass discrimination, and the cross section for molecular ion formation.

Generally, for the present experimental conditions, species could be detected in unfavorable cases at partial pressures of 10^{-7} atm and in favorable cases at 10^{-8} atm. In unusual cases, the sensitivity of the instrument can be somewhat less as, for example, with $NaReO_4$ vaporization. Here, the $NaReO_4$ molecule fragments under electron impact to yield mainly Na^+ and only about 0.1% of the ions produced are $NaReO_4^+$. As the $NaBO_2$ glass vapor species also produces a high intensity of Na^+, this ion cannot conveniently be used as a measure of $NaReO_4$ and a partial pressure of $NaReO_4$ as high as 10^{-5} atm may be required for detection as $NaReO_4^+$. This problem could possibly be circumvented in future studies by using an electron ionizing voltage high enough to produce fragments such as ReO_3^+ at less obscured mass positions.

2.5 Glass Vaporization in Vacuum

2.5.1 Observations on Li, Na, and Cs-containing Species

Several series of measurements were made on the simulated nuclear glass. A series represents a sequence of experiments (runs) using the same portion of the glass sample. Results for each series were reasonably reproducible and two representative series are reported here in detail. A number of experimental runs were made for each

series, each run consisting of experimental pressure-temperature points. For each run the sample temperature was increased from room temperature, or a lower idling temperature where vaporization was negligible, and data points were then obtained with an increasing temperature chronology.

Mass spectral ions observed in the temperature range from 800 to 1150 °C, at 30 eV ionizing energy, included Na^+ (23 amu), $NaBO_2^+$ (66), Li^+ (7), $LiBO_2^+$ (50), Cs^+ (133), O_2^+ (32), and the associated isotopic species. A typical mass spectrum in bar-graph form is given in figure 3. Note that the intensities are plotted on a logarithmic scale. Also, isotopic peaks at m/e of 6, 48, 49, and 65 amu have been omitted for the sake of clarity. Both Li^+ and Na^+ ions are fragments from metaborate precursors. This assignment is supported by the invariance of the ion intensity ratio of M^+/MBO_2^+ with temperature and by the high appearance potentials of Li^+ and Na^+. As shown by the ionization efficiency curves in figure 4, the observed appearance potentials of Li^+ and Na^+ are 10.0 ± 0.5 and 9.0 ± 0.5 eV, respectively, as compared with the corresponding values of 5.4 and 5.1 eV for ionization from the elements. Also, the form of each curve is indicative of a single molecular precursor. By analogy with the electron impact behavior of $NaBO_2$ and $LiBO_2$, it is considered likely that Cs^+ is also produced by electron impact fragmentation of the metaborate precursor, $CsBO_2$. Gorokhov et al. [1971] observed M^+/MBO_2^+ ratios at 70 eV for Li, Na, and Cs metaborates of 0.48, 3.30, and 32.7, respectively. These ratios are likely to be higher than those for 30 eV. However, the trend suggests that even at 30 eV the low Cs^+ intensities observed in the present study would preclude direct observation of $CsBO_2$ as $CsBO_2^+$.

The release of O_2 from the glass melt (see fig. 3) is attributed mainly to reduction of the Fe_2O_3-Fe_3O_4 dissolved in the melt.

A small amount of Cl (0.1 wt.%) was indicated in the nominal glass composition. Therefore a search was made, at a reduced temperature, for the relatively volatile alkali chlorides. No significant signals were noted for $LiCl^+$ (40 amu), $NaCl^+$ (58), and Cs^+ (from fragmentation of CsCl). It is possible that most of this Cl was lost during the glass preparation.

Conversion of ion intensity to species partial pressure data was made using the parameters defined by equation (2.3) and which are listed in Table 2. For series I, the first four runs were obtained using a single mass spectrometer sensitivity calibration and mass discrimination curve. After the fourth run, the spectrometer tuning was changed to expand the observable mass range. The fifth run of the Series I data was obtained using a second mass calibration and the new mass discrimination curve. These new calibrations were also used for the series II data. We have assumed that $LiBO_2$, $NaBO_2$, and $CsBO_2$ each have the same total ioization cross section value, estimated as 2.4 (πa_o^2 units). The partial cross sections (corrected for fragmentation) are given in table 2, except for $CsBO_2$ where no $CsBO_2^+$ was observed. Values of k_i were obtained using the mass spectrometric constants given in table 2, together with the experimental $\Sigma I_i^+ \Delta t \cdot T^{\frac{1}{2}}$ values and the observed weight loss data.

A check on the internal consistency of partial pressure data can be made by comparison of calculated weight loss data with the upper limit imposed by the sample composition. Table 3 lists the calculated weight loss by vaporization (using eq. 2.6) of the major oxide components together with the initial concentration of each oxide. The calculated weight losses are reasonably consistent with the sample composition except for O_2. In this case more O_2 was lost than was initially present,

Table 2

Mass Spectrometric Constants Used for Ions
Over Simulated Nuclear Waste Glass

ion	m/e	Series I (Runs 1-4) A	τ	σ[a]	Series I (Run 5) and Series II τ	σ
Li	7	0.925	0.97	1.98	0.83	2.26
Na	23	1.00	0.97	2.14	0.97	2.33
O_2	32	1.00	0.87	1.20	0.91	1.20
$LiBO_2$	50	0.742	0.64	0.42	0.88	0.14
$NaBO_2$	66	0.802	0.53	0.26	0.87	0.08
Cs	133	1.00	0.29	2.40	0.70	2.40

[a]Units of πa_o^2, e.g., see Bonnell and Hastie (1979).

assuming reduction of Fe_2O_3 to Fe_3O_4 as the only source of O_2. This effect was also noted in the TMS studies (section 3). It is likely that a secondary source of O_2 is present in this glass. For the series II data the calculated amount of $CsBO_2$ lost is slightly greater than the total amount present. Considering the uncertainties in ionization cross sections and sample composition, the agreement between observed and calculated losses is satisfactory.

The experimental partial pressure versus temperature data are plotted in figures 5 to 10. Several distinctive features are common to each of these figures. Note in figure 5, for instance, that the initial run 1 data show anomalously high pressures at low temperatures. Also, note the tendency for the observed pressures to decrease slightly with time e.g., as in the run 5 versus run 1 data. The initial high pressure effect may be due sample inhomogeneity. It is likely that small surface regions exist with higher concentrations of volatile components than for

Table 3
Comparison of Calculated Weight Loss Data with Sample Composition (in mg)

	Series I (Initial sample weight 263.1 mg)						Series II (Initial sample weight 418.4 mg)		
	Runs 1-4		Run 5						
	Borate Loss	Oxide Equivalent	Borate Loss	Oxide Equivalent	Total Loss[a]	Total Oxide Present	Borate Loss	Oxide Equivalent	Total Oxide Present
Na_2O	7.89	3.71	3.30	1.55	5.3	26.1	12.36	5.82	42.3
Li_2O	4.33	1.30	2.16	0.65	2.0	13.4	5.74	1.72	21.3
Cs_2O	0.06	0.05	0.04	0.03	0.08	0.26	0.62	0.50	0.42
B_2O_3	---	7.22	---	3.27	10.5	19.2	---	10.69	30.5
O_2	1.43	1.43	1.00	1.00	2.43	1.1	3.39	3.39	1.81

[a]Summation of Runs 1-5, oxide equivalent.

the bulk sample. The decrease in $NaBO_2$ pressure with time results from the significant depletion of the bulk B_2O_3 concentration due to metaborate vaporization. This observation further confirms that Na vaporization occurs as the metaborate since the B_2O_3 concentration is reduced much more than the Na_2O content. The partial pressure curve shown in figure 5 results from a least squares analysis of the runs one to four with the anomalous three lowest temperature data points from run 1 omitted. The pressure of $NaBO_2(g)$ over pure $NaBO_2(\ell)$ obtained from the JANAF [1971] tabulation is also given in figure 5 for comparison. From the ratio of pressures from these curves, the activity of $NaBO_2$ in the simulated nuclear glass is approximately 0.01 with a slight temperature dependence.

The vaporization curves for $LiBO_2$ and $CsBO_2$ species are given in figure 6. A least squares curve through the $LiBO_2$ data was obtained from the run 1-4 data neglecting the two lowest temperature points of run 1. Comparing this curve with that for pure $LiBO_2(\ell)$, obtained from JANAF [1971], indicates that the activity of $LiBO_2$ in the SNW glass is about 0.1, with some temperature dependence. The $CsBO_2$ data in figure 6 were obtained in series I, runs 4 and 5. We did not observe Cs^+ until the fourth run in this series and it is likely that the sample was somewhat depleted in $CsBO_2$ prior to the measurements. This depletion effect is very apparent at $10^4/T = 7.50$ (see fig. 6). The least squares curve through these data is based on the four lowest temperature points obtained from run 4. At 1200 K, the activity of $CsBO_2$ in the melt is about 4×10^{-6} based on the $CsBO_2$ pressure over pure $CsBO_2$ as given by Gurvich and Veits [1983].

Figure 7 shows the observed O_2 pressure versus temperature data. The least squares curve was obtained by neglecting the five lowest

temperature points. From the reasonable comparison with the literature curve [JANAF, 1971] for reduction of $Fe_2O_3(c)$ to $Fe_3O_4(c)$ it appears likely that reduction of Fe_2O_3(in solution) to Fe_3O_4(in solution) is a primary source of O_2 over the SNW glass.

Similar data were obtained for the series II experiments, as shown in figures 8 to 10. In these figures, the series II data points are compared with the least square curves from series I (except for O_2) to indicate the degree of experimental reproducibility for separate glass samples. While the O_2 data for the two series, as given in figures 7 and 10, are similar, an exact comparison is meaningless owing to the variation of Fe oxidation state with time, i.e., run chronology.

Note in figure 8 that the run 1 data show the characteristic high $NaBO_2$ pressures at low temperatures. The positive deviation (from the least squares curves) in pressures during the initial heating is characteristic of all the data. During the high temperature component of run 2 an instability was observed in the Na^+ signal. This effect was characterized by signal increases of a factor of two, or more, for short periods of time (tens of seconds) but would return to the original level. These instabilities could be associated with the concomitant release of a noncondensible gas from the sample as was indicated by pressure increases on the ionization gauge. Note however, that the run 3 data was well behaved and lies quite close to the least squares line from the series I data. Also, the $LiBO_2$ data shown in figure 9 agree well with the series I least squares curve.

The data comparison in figure 10 for $CsBO_2$ indicates the series II data to be about a factor of four greater than those based on the least squares line from the series I data. Since the amount of

$CsBO_2$ calculated to have been lost from the sample is slightly greater than the amount originally present (see Table 3) we conclude that the Series II $CsBO_2$ pressures are anomalously high. However, the series I data are probably too low because the Cs^+ data was not observed until runs 4 and 5. Hence we consider an average of these two series to best represent the $CsBO_2$ partial pressure data. This procedure increases the pressure from the series I data by a factor of two and the accepted curve is shown as the dashed line in figures 6 and 10. This curve also agrees well with that obtained from the TMS measurements (see Section 3).

2.5.2 Search for Ru, Re, and Sr-containing Species

Attempts were made during the vacuum vaporization experiments to detect the ions Ru^+, RuO^+, RuO_3^+, RuO_4^+, and Re^+, ReO^+, ReO_2^+, ReO_3^+, and $Re_2O_7^+$ without success, even at temperatures as high as 1500 °C. No attempt was made to observe SrO^+ or Sr^+, based on thermodynamic arguments presented in Section 4.1.

From the thermodynamic arguments presented in Section 4.1, $NaReO_4$ is indicated as the most likely vapor form of Re. Also, this species is likely to have a sufficiently high partial pressure to completely remove Re from the glass during the vacuum vaporization measurements. However, the $NaReO_4$ species fragments extensively on electron impact to form Na^+ and parent ions form only a small fraction of the total ion production. The small Na^+ ion signal resulting from fragmentation of $NaReO_4$ would be completely masked by the large Na^+ signal resulting from fragmentation of $NaBO_2$. A similar problem exists for fragmentation of $LiReO_4$.

The thermodynamic analysis given in Section 4.1 for Ru vaporization indicates RuO_3 and RuO_4 as the likely vapor species but their partial pressures are predicted to be below the KMS detection limit.

2.6 Glass Vaporization in H_2O Atmosphere

Volatile hydroxide species are known for all of the pertinent oxides in the SNW glass system, e.g., see JANAF [1971], Jackson [1971], and Hastie [1975]. However, the extent to which water vapor will react with these oxides, in the reduced activity glass form, to yield hydroxide vapor species cannot be accurately predicted from existing thermodynamic data. Also, our previous experience with reactive gas-glass systems indicates that thermodynamic equilibrium may not be attained [Hastie, et al. 1982]. Hence, gas inlet KMS (GKMS) experiments were carried out to determine if water vapor would enhance the vapor transport of the SNW glass. Water vapor pressures up to about 10^{-4} atm were used for these measurements.

2.6.1 H_2O-B_2O_3 Test Case

The GKMS approach was tested using the well known H_2O-B_2O_3 reaction system (JANAF, 1971). Prior to H_2O introduction into the cell, containing pure B_2O_3, the mass spectrometer sensitivity calibration was checked using the known (JANAF, 1971) vapor pressure of $B_2O_3(g)$ over $B_2O_3(\ell)$. Our results agreed to within about 20 percent of the JANAF [1971] evaluation of previous literature data.

In the presence of H_2O, the principal reaction is

$$\tfrac{1}{2}B_2O_3(\ell) + \tfrac{1}{2}H_2O(g) = HBO_2(g) \quad . \qquad (2.7)$$

The degree of reaction was monitored mass spectrometrically using the H_2O^+ and HBO_2^+ ions as indicators of the H_2O and HBO_2 partial pressures, respectively. Isothermal measurements of the dependence of the HBO_2^+ ion intensity on that for H_2O^+, with variable H_2O pressure, were used to demonstrate attainment of a steady state, as shown in figure 11. The experimental slope of 1.1 ± 0.1 compares favorably with the theoretical slope of 1.0.

Equilibrium constant data for reaction (2.7) are shown in figure 12. The experimental data compare favorably with the JANAF [1971] curve, which is based on the mass spectrometric results of Meschi et al. [1960]. For this comparison, we used the same ionization cross section estimates as Meschi et al. [1960].

2.6.2 H_2O-Glass Experiments

Experiments analogous to the B_2O_3-H_2O test case gave negative results and the thermochemical calculations presented in Section 4 indicate that any hydroxide species formed are likely to be below the instrumental detection limit. It is also possible that the water-SNW glass system does not readily attain equilibrium, as we have found in other glass studies (Hastie et al., 1982).

3. TRANSPIRATION MASS SPECTROMETRY

3.1 Basis of Technique

The Transpiration Mass Spectrometry (TMS) technique has been described in detail elsewhere [Bonnell and Hastie, 1979]. Basically, the method combines the high pressure sampling mass spectrometry and classical transpiration techniques. High pressure sampling is accomplished by free-jet expansion from a static region into a region of high pumping speed [Kantrowitz and Grey, 1951]. This is the only technique with the potential for preserving the chemical integrity of the gas sample during the expansion and molecular beam-forming process. The free-jet expansion occurs through a small orifice (diameter range, 0.008 to 0.03 cm) of controlled geometry into a region of low pressure. During this expansion process, most of the internal thermal energy converts to translational energy, i.e., to directed motion along the jet axis. For very high expansion ratios, this process occurs on a shorter time scale than for chemical reaction rates, thus generating a beam free from intermolecular interaction. This chemically "frozen" beam can then be conveniently analyzed by mass spectrometry.

Analysis of the gas dynamic aspects of the TMS process yields a simple relationship between the mass spectrometric ion intensities and species partial pressures. This relationship has the same form as equation (2.2) used in Knudsen effusion mass spectrometry. However, with TMS the sensitivity constant k has a slight temperature dependence and an internal calibration is made at each data point using the carrier gas signal and pressure for reference. Use of the classical transpiration

equation can also be made for partial pressure measurement once the realtive concentrations of different vapor species is established.

The primary equation for transpiration is

$$P_i = [n_i/(\Sigma n_i + \Sigma n_c)]\ P_t \qquad (3.1)$$

where , for species i and carrier gas c, P_i is the partial pressure, n the number of moles, and P_t the system total pressure ($\sim P_c$).

An upper pressure limit to TMS is determined mainly by experimental limitations in maintaining vacuum in the expansion chamber. We have used the technique to 10 atm but the normal optimum pressure range is in the region 0.1 to 0.5 atm. Thus TMS extends the 10^{-4} atm limit of KMS by many orders of magnitude and allows for higher temperature and reactive gas pressure studies. Typical gas residence times for TMS and KMS are 20 s and 0.04 s, respectively. This difference is particularly useful in revealing nonequilibrium phenomena by comparisons of TMS and KMS data.

3.2 Apparatus

The basic arrangement of the High Pressure Mass Spectrometer (HPMS) system with the transpiration inlet system is shown in figure 13. The vacuum system is aluminum walled and is partitioned into two differentially pumped stages. Stage I contains the transpiration reactor. This stage is pumped by a 6 inch diffusion pump (Varian/NRC VHS-6) with a Granville-Phillips model 270-6 high-throughput cold trap close-coupled to the base of the vacuum chamber for maximum conductance. The backing pump system for this stage consists of a Roots blower (Leybold-Hereaus

model WA 250) placed in series with a two stage rotary vane pump (Sargent-Welch 1375) to maintain the critical backing pressure of the diffusion pump in the presence of high gas loads. This arrangement assures that the diffusion pump stack will continue to pump at near its rated speed into the 10^{-5} atm range. A single-axis adjustable combination valve/shutter separates the two vacuum chambers. The differential pump aperture used is 0.05 cm diameter, and is located approximately 4 cm from the sampler orifice. This aperture is located in a shutter which also acts as a stage isolation valve.

A tantalum foil (0.005 cm) radiation furnace, driven at AC currents to 400 amperes, provides heat to the transpiration sampler. With a new element, temperatures as high as 1700 K can be achieved in the sampler. Adjustable passive tantalum radiation shields are used to maintain a near constant temperature profile in the boat to skimmer region. The furnace region is surrounded by a water-cooled copper shroud to prevent condensibles (oil, high temperature species, etc.) from entering the mass spectrometer chamber.

In the Stage II mass spectrometer section, a high vacuum is maintained by a 4-inch diffusion pump stack similar to the 6-inch stack of stage I, but without the Roots blower. Full-load vacuum in this stage is better than 5×10^{-9} atm. The beam modulation chopping system is also located in this chamber. A 24 tooth wheel driven by a degassed ac syncronous motor is used to provide variable frequency beam modulation. Usually, chopping frequencies of about 700 hertz are chosen to minimize syncronous interference at the 60 hertz line frequency and to provide species sensitive phase information. The mass spectrometer used is an Extranuclear Laboratories Component quadrupole system, based on an EL

model 270-9 quadrupole mass filter, a crossed beam configuration EL ion source (Model 041-1)--modified to improve isolation, collimation and ionizing energy spread--and a Galileo Electro-Optics model 4801 channeltron multiplier. The mass spectrometer assembly is mounted on a semi-kinetic 3 point mount which allows for three axis alignment of the ionizing region with the molecular beam.

Figure 14 shows the essential details of the transpiration reactor with its removable boat-carrier assembly. With the exception of the thermocouple alumina insulator, which is located upstream from the gas baffle to minimize reaction with the sample vapor, the entire assembly is constructed of platinum metal. For glass sampling, the conical orifice and skimmer assembly shown have been replaced with a more robust capillary nozzle detailed in figure 15. A typical temperature profile within the sampler is shown to scale with the sampler. The capillary sampler has proven to be as faithful a beam generation device as the more traditional conical orifice [Bonnell and Hastie, 1979].

For preparation and control of gas mixtures, we use a group of Tylan Corp. mass flow meters and controllers (FM360 and FC260, respectively) attached to an NBS-designed backflow protected mixing manifold. Individual range selection allows gas mixtures to be prepared at room temperature with the reactive gas mole fractions varying from 10^{-6} to 10^{-1}. For water vapor additions the dry mixed gas is fed to commercial water calibrators (either Ondyne models 10 or 14). The water content of the prepared mixture is monitored by two high sensitivity aluminum oxide/gold hygrometers (Ondyne model DY143T/model 1400) with a calibrated accuracy of better than ± 2 °C (about ± 20% in vapor pressure). Total system pressure is monitored at the gas inlet to the sampler mount

using a Rosemount model 1332A4 capacitance manometer transducer excited and read by an NBS built readout system.

3.3 Instrument Calibration

Calibration of the TMS system is, for the most part, an analogous process to that used for the KMS system as described in Section 2.3. For calibration of mass discrimination effects an identical procedure to that for KMS was used. To convert ion intensity and mass-loss data to partial pressures using the transpiration equation (3.1), the following calibration procedures are necessary.

Calibration of the system pressure gauge [P_t in eq. (3.1)] is accomplished by comparison with a known standard gauge, and P_t is reproducible to better than 0.003 atm. The term in moles of carrier gas [n_c in eq. (3.1)] is determined by direct measurement of the mass flow of each gaseous component, and a separate measurement of the total mass flow into the system. Several independent calibration methods are used for the flow meters and controllers: (1) comparison with previously calibrated mass flow meters; (2) direct volumetric calibration against a well characterized "wet-test" meter; (3) direct volumetric calibration of flow into a mercury-sealed piston gas burette; and (4) direct volumetric collection over saturated fluid. These various techniques suffice to assure reproducible flow measurements to within the accuracy specifications of the Tylan meters used, i.e., well within 1% of full scale. Most mixtures are made using at least 10% of full scale, hence component composition and n_c are known to within a few percent.

For vapors containing more than a single type of molecular species, such as those over the present glass system, a partitioning of the total mass transport is needed. This partitioning is achieved by integration of the observed ion intensities with the constraint that the sum of individual species mass transport equals the gravimetric total mass loss. This procedure leads to n_i values for use in eq. (3.1). The individual species molar transport partitions q_i are given by

$$q_i = \sum_i \Delta q_i(T) = \frac{C_i}{R} \sum_T \left(\frac{f_c}{I_c} \cdot I_i \cdot \frac{V_s}{273} \Delta t(T) \right) \qquad (3.2)$$

where, for species i,

q_i is proportional to the number of moles of species i transported during an entire series of experiments;

$\Delta q_i(T)$ is an individual species molar partition at temperature T;

C_i is the factor, $(\sigma_c \tau_c)/(\sigma_i \tau_i)$, which accounts for relative transmission and ion cross sections effects, where σ is the total ionization cross section (where fragment ions are involved, direct summation or average ion ratios are used to allow use of total ionization cross sections) and τ is the mass dependent relative transmission factor for the quadrupole mass spectrometer and gas expansion system;

R is the universal gas constant 82.057 (cm^3 atm/mol K);

f_c is the product of isotopic fraction and gas fraction of component c in the gas mixture, i.e. the actual fraction of gas observed at mass position c;

I_c is the ion current of carrier gas component c--this creates approximate correspondence between q and n, and normalizes beam characteristics which change with temperature and pressure;

I_i is the species ion current, appropriately converted (via fragment ion summation, or scaling by ion ratios) to a total ion current for species i;

V_s is the flow rate in standard (P=1 atm, T = 273.15 K) cubic centimeters of total carrier gas per minute (sccm);

273 is 1 atm/273.15 K, the reference condition for flow calibration;

$\Delta t(T)$ is the elapsed time in minutes for a run segment at constant temperature, T.

In eq. (3.2), each variable is considered a function of the system temperature, T, and the summation is carried out over every observed temperature point. When the total mass loss of the system is measured at the conclusion of a series, the above partitions can be converted to pressure by computing a proportionality factor, k, from the equation:

$$\text{weight loss (gms)} = k\sum_i q_i \cdot M_i \qquad (3.3)$$

where M_i is the species molecular weight and k the factor which yields actual moles from the q_i obtained from ion current measurements. Individual values of $\Delta n_i(T)$ are obtained by multiplying the calculated $\Delta q_i(T)$ of eq. (3.2) by k. These values are then used in eq. (3.1) to compute $P_i(T)$ from the ion intensity observations.

A second approach to converting ion intensity to partial pressure data is used when relative ionization cross sections are considered more reliable than total mass loss data. Here, eq. (2.2) is used but with k_i measured at every data point using the relationship

$$k_i = \left(\frac{P_c}{I_c T}\right)\left(\frac{\sigma_c}{\sigma_i}\right)\left(\frac{\tau_c}{\tau_i}\right)\left(\frac{1}{\bar{S}}\right), \qquad (3.4)$$

where $\bar{S}$ is an apparatus dependent small correction factor (= 0.6) which results from scattered carrier gas reentering the molecular beam [Bonnell and Hastie, 1979]. For the present studies, where the glass vapor mass spectra were relatively complex, preference was given to the calibration approach based on equations (3.1) to (3.3).

3.4 Detection limits

TMS detection limits are strongly controlled by beam formation characteristics and the amount of background gas present in the beam-forming and mass spectrometer chambers. The beam, as formed, is narrowly collimated by Mach focussing and by restrictive orifices. However, the beam formation process leads to a large increase in background pressure in the mass spectrometer chamber, generally in the 10^{-9} to 10^{-8} atm range. Beam spread during transit to the mass spectrometer reduces the total beam number density at the ion source to the order of 10^{12} particles cm^3, about four orders of magnitude above the background number density. Modulation of the beam allows reliable detection of signals two to three orders of magnitude below prevailing background DC signals. In favorable cases, this leads to detection limits of approximately 0.3 to 1 ppm (relative to 1 atm). In unfavorable cases, e.g., at mass positions corresponding to scattered carrier gas components or strong hydrocarbon background levels, detection limits lie in the 10 to 100 ppm range. Mass positions coincident with major carrier gas isotopes are totally masked. However, carrier gas selection is made to avoid mass coincidence with minor species of interest. Mass positions adjacent to the major carrier gas isotopes usually evidence some residual modulation due to

incomplete resolution. For instance, ppm detection at 27 amu requires a resolution with better than 0.001% cross talk in the presence of 28 amu N_2 carrier gas. In the present study, unit resolution conditions were used over the whole mass range, with adjacent peak cross talk of less than 0.1 percent.

In practice, sensitivity limits can be reliably estimated from the magnitudes of DC ion intensity and non-phase-locked AC signals. For the results presented here (Section 3.5), the lowest partial pressure values represent signal-to-noise (or background) levels in the range 2 to 5. At the higher partial pressures given these noise levels are an insignificant source of error.

3.5 Glass Vaporization in N_2 Atmosphere

TMS measurements of SNW glass vaporization were made using ultra high purity N_2 carrier gas (at 0.3 atm) and higher temperatures than those for the KMS vacuum vaporization experiments. The mass spectral features were generally similar to those found by KMS, as outlined in Section 2.5. Several distinctly new features were also noted and these can be attributed to the beam isentropic cooling and reduced mass transport effect characteristic of the TMS method. As we have noted in earlier studies [Bonnell and Hastie, 1979], the distribution of parent to fragment ion intensities can differ between KMS and TMS studies due to beam cooling with the latter technique. Thus in the present study we observe, for instance, Li^+ (7 amu)/$LiBO_2^+$ (50 amu) ratios of 30 for TMS as compared with 9 for KMS. However, the molecular precursor assignment, as $LiBO_2$, and the value of the total ionization cross section are not influenced by this effect.

The mass transport rates characteristic of TMS are much lower than for KMS and this leads to differences in the early vaporization stage of a new glass sample, as noted elsewhere [Hastie et al., 1982]. Examples of such effects, which are not characteristic of the bulk glass properties but rather of impurities, are revealed in figures 16 through 18. Note in figure 16 that the $Na^+/NaBO_2^+$ ratio varies significantly with temperature and time. If $NaBO_2$ was the sole precursor of Na^+, this ratio would be invariant with temperature and time. The results can be analyzed in terms of two additional sources of Na as manifested in the Na^+ signal. During the early stages of vaporization, as represented by the $Na^+/NaBO_2^+$ data points at 1400 to 1500 K in figure 16 and the Na atom data points at 1300 to 1500 K in figure 17, most of the observed Na^+ results from Na. The most likely source of this Na is from decomposition of residual Na_2CO_3, i.e.,

$$Na_2CO_3\ (\ell) = 2Na + CO_2 + \tfrac{1}{2}O_2.$$

Observation of CO_2 and O_2 during this period supports this argument as shown in figure 18. We have shown in earlier silicate glass vaporization studies that this effect results from a finite Na_2CO_3 solubility in glass which results during glass preparation with alkali carbonate reactants [Hastie et al., 1982]. At the higher temperatures and later vaporization times, when the carbonate impurity is essentially depleted, a second Na-producing reaction occurs,

$$Na_2O\ (\text{in solution}) = 2Na + \tfrac{1}{2}O_2.$$

The curve labeled Na_2O in figure 17 shows the Na pressure determined for this process. No analogous processes were noted with the Li data, i.e., both Li^+ and $LiBO_2^+$ are attributed to a single precursor, $LiBO_2$.

The observed borate ion signals were corrected for fragmentation to alkali ions by assuming that the minimum fragmentation ratio (see fig. 16) corresponded to the borate fragmentation process alone. These ratios were corrected for isotopic abundance and the borate ion intensities multiplied by the corrected ratio to obtain a total borate ion signal. As was the case with the KMS results, the Cs^+ precursor is assigned as $CsBO_2$. In order to convert ion current to partial pressure data, ionization cross section corrections for the relative efficiency of ionizing various species must be made. For the alkali metaborates, which are the major vapor transport species, an estimated σ_i value of 2.4 was used [units πa_o^2, see Bonnell and Hastie, 1979]. As noted in the KMS studies, considerable fragmentation occured even at 30 eV ionizing energy.

The alkali metaborate partial pressures obtained by this analysis are summarized in figures 17 and 19. Note in figure 19, the excellent agreement between the TMS and extrapolated KMS data for each metaborate species. Such agreement supports the TMS analysis of the Na^+ signal in terms of the three competing processes. Also, the linear fit to both the TMS and KMS data sets is consistent with the thermodynamic basis of these Clausius-Clapeyron type plots and allows for accurate extrapolation to temperatures beyond the experimental results. The agreement between the TMS and KMS data is also good evidence of thermodynamic equilibrium and of the absence of surface segregation effects. These arguments are based on the different gas residence times and material transport rates characteristic of the two techniques, as discussed in Section 3.1. Surface segregation of volatile species have been reported in a sodium borosilicate melt [Wenzel and Sanders, 1982].

It is conceivable that the Cs^+ signal may also result from several processes analogous to those for Na^+. However, at the relatively low temperatures of the KMS experiments no evidence for additional sources of Cs^+ was found. Also, the good agreement between the KMS extrapolated $CsBO_2$ curve and the higher temperature TMS data is reasonable evidence of the absence of competing reactions leading to additional Cs^+ signals.

It is interesting to note, though thermodynamically fortuitous, that the $CsBO_2$ partial pressures of SNW glass are similar to those for Cs over SYNROC ($Ba_{0.9}\ Cs_{0.1}\ Al_2\ Ti_6\ O_{16} \cdot TiO_2$) as reported very recently by Carpenter, et al. [1983]. Also, the value of $P(CsBO_2)$ at 1075 °C lies between that of P(Cs) over the minerals $CsAlSiO_4$ and $CsAlSi_2O_6$ [Odoj et al. 1979].

3.6 Glass Vaporization in H_2O-O_2-CO_2-N_2 Atmosphere

In the industrial glass process the off-gas contains components which are potentially reactive with the glass constituents. These include, with mole fractions in parentheses, H_2O (0.85), O_2 (0.02), CO (0.008), H_2 (0.008), CO_2 (0.01), and minor amounts of N- and S-containing species. This room temperature composition is clearly nonequilibrated. At high temperatures we need only specify the H_2O, O_2, and CO_2 concentration at thermodynamic equilibrium. This result can be seen in table 4 where the calculated composition of an <u>equilibrated</u> off-gas mixture is given as a function of temperature. Note that at a representative temperature of 1250 K, CO_2, O_2, H_2O, and N_2 are the only thermodynamically significant components.

Table 4

Calculated Equilibrium Composition (mole fraction) of Off-gas Mixture at 1 atm[a]

Input Composition (moles)[b]:

H_2O (0.8555), N_2 (0.09023), CO_2 (0.01244), O_2 (0.02378), CO (0.008359), H_2 (0.007588).

Temperature K

	2500	2000	1500	1250	1000	333
CO	3.77-3[c]	2.09-4	7.80-7	8.59-9	9.69-12	0.00
CO_2	1.66-2	2.07-2	2.09-2	2.09-2	2.09-2	2.09-2
H_2	2.99-2	1.92-3	1.26-5	2.29-7	5.81-10	0.00
H_2O(L)	0.00	0.00	0.00	0.00	0.00	8.39-1
H_2O	8.01-1	8.64-1	8.69-1	8.69-1	8.70-1	3.09-2
O_2	2.56-2	1.67-2	1.68-2	1.69-2	1.69-2	1.68-2
N_2	8.79-2	9.12-2	9.18-2	9.18-2	9.18-2	9.19-2
NO	2.81-3	7.81-4	1.28-4	3.00-5	3.41-6	1.19-15
NO_2	7.97-7	3.55-7	1.85-7	1.10-7	5.12-8	5.39-11

[a]Calculated using the NASA CEC 76 computer program of Gordon and McBride [1971].
[b]Based on Dupont analysis of off-gas composition at room temperature [Soper, 1982].
[c]Computer notation, 3.77-3 = 3.77×10^{-3} mole fraction.

The following mole-fraction mixture was used in the TMS experiments to approximate the off-gas reactivity: N_2 (0.67), O_2 (0.18), CO_2 (0.15), and H_2O (0.1). The TMS results with this gas mixture indicated no significant enhancement of alkali vapor transport, due to hydroxide formation, with detection limits of 5 ppm for LiOH and 20 ppm for NaOH. The higher NaOH detection limit, resulted from the unavoidable presence of Ar impurity (also 40 amu) in the gas mixture. Vaporization of the lithium and sodium metaborates was essentially the same as for the pure N_2 runs, to within the mass spectrometric reproducibility of ca. 20%. No increase in either sodium or lithium ion currents attributable to fragmentation from a hydroxide was found. From our previous experience with TMS studies of alkali hydroxides [Hastie, et al., 1982, 1983], only moderate fragmentation occurs, and the detection limits at the parent ion can be considered reliable. .

With these reactive atmosphere conditions, a higher than normal hydrocarbon background was present, particularly at high temperature. This background raised detection limits by as much as an order of magnitude at the Cs^+ ion mass position. Some suggestion of an atmosphere induced increase in Cs^+ intensity was noted, but the results are considered inconclusive due to the increased background level. This hydrocarbon background could have originated as a low level relatively tightly bound constituent of the glass, or, as an abnormal apparatus background.

This TMS observation of alkali vapor transport insensitivity to the presence of H_2O vapor is consistent with a similar observation from the KMS experiments (Section 2.6). Previous experiments on a sodium borosilicate glass [Wenzel and Sanders, 1982] and various sodium, potassium borosilicate glasses [Gray, 1980], also showed an unexpected non-effect of H_2O on alkali vapor transport.

4. Thermodynamic Estimates

4.1 Glass Vaporization in Inert Atmospheres

The only radionuclide element observed by the present mass spectrometric studies is Cs, present in the vapor as $CsBO_2$. From the mass spectrometric detection limits, partial pressure limits for the other radionuclides at temperatures as high as 1500 °C are in the region of 10^{-7} atm with an inert atmosphere and 10^{-6} atm with H_2O or the reactive gas mixture present. Using the experimental activity results for the various glass components, together with auxiliary thermodynamic data from the literature, it is possible to calculate approximate radionuclide concentrations in the vapor phase, as follows.

4.1.1 Cs

As this radionuclide was observed experimentally, the data can be used to indicate the quality of the thermodynamic estimates. The KMS results indicate the activity of $CsBO_2$ as

$$a(CsBO_2)_{obs} = 4 \times 10^{-6} \text{ at } 1200 \text{ K.}$$

If we assume that Cs is present primarily as $CsBO_2$ (ℓ) in the glass, and that this component mixes ideally, then from the glass composition (see Table 1) the activity would be

$$a(CsBO_2)_{calc} \sim 4 \times 10^{-4}.$$

On this basis, the vapor phase concentration of Cs (as $CsBO_2$) would be two orders of magnitude higher than observed, i.e.

$$P(CsBO_2)_{calc} \sim 10^{-6} \text{ atm at } 1200 \text{ K}$$

whereas

$$P(CsBO_2)_{obs} \sim 10^{-8} \text{ atm at 1200 K.}$$

4.1.2 Sr

An upper limit vapor concentration can be calculated assuming ideal mixing of SrO (ℓ) in the glass. Thus the activity of SrO (ℓ) is 0.0006 and, from JANAF [1971],

$$P(SrO) < 1.4 \times 10^{-11} \text{ atm at 1800 K.}$$

Also, in the presence of 1×10^{-5} atm O_2, as produced by Fe_2O_3 decomposition (see Section 2.5), we calculate

$$P(Sr) < 3 \times 10^{-12} \text{ atm at 1800 K.}$$

4.1.3 Re

The compound Re_2O_7 has a boiling point of 635.5 K [Wicks et al. 1963]. If we assume that Re_2O_7 is dissolved in the glass (with a mole fraction of 0.0001) then the vapor pressure at this temperature would be 1×10^{-4} atm. Hence, Re_2O_7 would be lost from the glass during the initial stage of an experiment. It seems more reasonable that Re would be incorporated in the glass as ReO_2, ReO_3 or, more likely, as $LiReO_4$ or $NaReO_4$. In the case of $LiReO_4$ and $NaReO_4$, the Re_2O_7 activity would be reduced far below the value given by the formal mole fraction.

Battles et al. [1968] have published definitive studies on ReO_2 and ReO_3 vaporization processes. Both of these phases vaporize to

produce a gas containing predominantly Re_2O_7. From their vapor pressure curve for the reaction

$$7/2\ ReO_2(s) = 3/2\ Re(s) + Re_2O_7(g) \qquad (4.1)$$

an extrapolated vapor pressure at 1500 K is 7.46 atm. As an approximation, we can neglect the thermodynamic difference between $ReO_2(s)$ and $ReO_2(\ell)$. Taking the mole fraction of ReO_2 in the solution to be 0.0002 and the activity of Re(s) equal to unity, the calculated partial pressure of Re_2O_7 at 1200 K is 7.31×10^{-13} atm. This pressure could be increased significantly if Re dissolves in the glass melt thereby reducing the activity significantly below unity.

The vaporization behavior of $NaReO_4$ has been established by mass spectrometry (Skudlarski et al., 1967). This salt evaporates to produce $NaReO_4$ monomers as well as dimers in the temperature range 700 to 800 K. Extrapolation of the monomer data to 1200 K and using 0.0002 as the mole fraction of $NaReO_4$, the calculated pressure is

$$P(NaReO_4) \sim 1.5 \times 10^{-7} \text{ atm at } 1200 \text{ K.}$$

4.1.4 Ru

For condensed RuO_2 in the presence of O_2 the important vapor species are RuO_3 and RuO_4, as shown by Schäfer et al. (1963). From their vapor pressure equations, with an RuO_2 mole fraction of 0.0005, an oxygen pressure of 10^{-5} atm and a temperature of 1500 K, the predicted partial pressure of RuO_3 is 5.3×10^{-9} atm. Similarly, the calculated partial pressure of RuO_4 is 3.1×10^{-12} atm. Thus vapor transport of Ru under the KMS experimental conditions is predicted to be undetectable.

However, for higher O_2 pressures, such as the likely off-gas value of 0.02 atm, the partial pressures of RuO_3 and RuO_4 are calculated to be 2.35×10^{-7} and 6.13×10^{-9} atm, respectively. Thus under melt conditions most of the Ru vapor transport would be due to loss via RuO_3.

Results of these thermodynamic estimates are summarized in figure 20.

4.2 Glass Vaporization in H_2O-O_2 Atmospheres

Within the experimental detection limits of KMS and TMS, the presence of H_2O or O_2 had no effect on the SNW glass vaporization process. Thermodynamic estimates of the likely influence of these reactive gases on the glass vaporization are as follows. Unless indicated otherwise, the thermodynamic tables for hydroxide vapor species given by Jackson [1971] and the JANAF [1971] tables have been used in the following calculations. Also, to simulate the likely off-gas composition we set $P(H_2O) = 0.1$ atm and $P(O_2) = 0.02$ atm.

4.2.1. Cs

The major influence of H_2O on Cs vapor transport can be expected to result from the reactions

$$MBO_2(\ell) + H_2O(g) = MOH(g) + HBO_2(g),$$

where M is Li, Na, or Cs. We can show thermodynamically that the Li case greatly outweighs the Na and Cs cases. Hence the Li reaction can be used to fix the system HBO_2 pressure. Using this pressure, the

experimental activity of $CsBO_2(\ell)$, the literature thermodynamic functions for $CsBO_2(\ell)$ [Gurvich and Veits, 1983], and the reactant thermodynamic functions, we calculate P(CsOH) data as given in figure 21.

4.2.2 Sr

The most volatile strontium hydroxide is $Sr(OH)_2$. For the assigned water vapor pressure of 0.1 atm, and an $SrO(\ell)$ mole fraction of 0.0006, the calculated $Sr(OH)_2$ partial pressure at 1500 °C is 3.5×10^{-9} atm. In this calculation it was assumed that a negligible difference would result from assuming that the properties of $SrO(\ell)$ are the same as SrO(s) at the reduced activity. Partial pressures of $Sr(OH)_2$ as a function of temperature are summarized in figure 21.

4.2.3 Re

Calculated partial pressures for the $HReO_4$ vapor species, from $NaReO_4(\ell)$ with an activity of 0.0002, are given in figure 21. The partial pressure of product NaOH was fixed by the reaction

$$NaBO_2(\ell) + H_2O = NaOH + HBO_2 ,$$

shown in figure 21.

4.2.4 Ru

The $Ru(OH)_2$ species is predicted to be the main hydroxide of Ru under the assigned conditions. However, as indicated in figure 21, the calculated partial pressures are extremely small. The possible

existence of higher oxidation state, more volatile, hydroxide species should not be discounted as the thermodynamic literature is sparse in this area.

5. Conclusions

The KMS and TMS experiments provide complementary, self consistent data for the major volatile species, $NaBO_2$, $LiBO_2$, and $CsBO_2$ as summarized in figure 19. Estimates based on thermodynamic arguments for the most likely oxide forms for the other radionuclides of interest are given in figure 20. Note that the $NaReO_4$ species may be even more important than $CsBO_2$. Both Ru and certainly Sr are indicated to have very low oxide volatility. In the presence of H_2O and O_2 a number of additional hydroxide species are predicted to be significant as shown in figure 21. However, the partial pressures of these species are still less than those of the oxide forms. As an interim conclusion from these observations, it appears likely that the glass off-gas atmosphere is of secondary importance to the condensed phase composition in controlling vapor transport. In view of the importance of metaborate vapor species, the concentration or, more particularly, the thermodynamic activity of boron oxide in the glass is of key significance.

The thermodynamic predictions of figures 20 and 21 should be refined in future studies to include

- o competition between competing reactions
- o effects of departure from ideal mixing

This refinement will need to incorporate direct experimental observations of radionuclide species. Figures 20 and 21 provide a useful guide to

the conditions needed in future mass spectrometric studies. Increased glass doping concentration levels of the radionuclide isotopes would increase the oxide and hydroxide partial pressures to well above the mass spectrometric detection limits. From the radionuclide partial pressure variation with glass concentration extrapolation to the composition of the present glass sample would be possible. Application of the ideal mixing of complex phases solution model [Hastie et al., 1981, 1983] to generalized predictions of SNW glass volatility and phase behavior should also be investigated.

6. Acknowledgments

A significant portion of this work was supported by contract with DuPont Atomic Energy Division, Savannah River Laboratory. The glass sample used was prepared and analyzed by DuPont. Discussions with Dr. Paul D. Soper of DuPont are acknowledged. Mr. Art Sessoms provided valuable technical assistance to the project.

7. References

Battles, J. E., Gunderson, G. E., and Edwards, R. K. (1968). J. Phys. Chem. 72, 3963.

Bonnell, D. W. and Hastie, J. W. (1979). "Transpiration Mass Spectrometry of High Temperature Vapors," in Characterization of High Temperature Vapors and Gases, Hastie, J. W., ed., NBS-SP 561, p. 357, U.S. Government Printing Office.

Cable, M. (1978). Materials Science Research 12, 399.

Carpenter, J. H., McMullen, J. C., Olmscheid, B. A., Chezick, P. A., and Olig, C. (1983). "Cesium Vaporization Losses from the SYNROC Mineral Barium, Cesium-Hollandite," Proc. Second Int. Conf. Ceramics in Nuclear Waste Management, Am. Cer. Soc., in press.

Gordon, S., and McBride, B. J. (1971). "Computer Program for Calculation of Complex Equilibrium Compositions, Rocket Performance, Incident and Reflected Shocks, and Chapman-Jouguet Detonations," (NASA Lewis Research Center, Cleveland, OH) NASA SP-273.

Gorokhov, L. N., Gusarov, A. V., Makarov, A. V., and Nikitin, O. T. (1971). Teplofiz. Vysok. Temp. 9, 1082. (English Trans.).

Gray, W. J. (1980). Radioactive Waste Management 1, 147.

Gurvich, L. V., and Veits, I. (1983). Thermodynamic Properties of Individual Substances, Vol. 4, Book 1, p. 525.

Hastie, J. W. (1975). High Temperature Vapors, Academic Press, NY.

Hastie, J. W., Horton, W. S., Plante, E. R., and Bonnell, D. W. (1981). "Thermodynamic Models of Alkali Vapor Transport in Silicate Systems, IUPAC Conf., Chemistry of Materials at High Temperatures, Harwell, U.K., August, 1981; High Temp. High Press, in press.

Hastie, J. W., Plante, E. R., and Bonnell, D. W. (1982). "Alkali Vapor Transport in Coal Conversion and Combustion Systems," in Metal Bonding and Interactions in High Temperature Systems with Emphasis on Alkali Metals, ACS Symp. 179, p. 543, American Chemical Society, Washington, DC.

Hastie, J. W., Bonnell, D. W., Plante, E. R., and Horton, W. S. (1983). "Thermodynamic Activity and Vapor Pressure Models for Silicate Systems Including Coal Slags," in Thermochemistry Today and Its Role in the Immediate Future, M. A. V. Ribeiro da Silva, Ed., Reidel Publ. Boston, in press.

Jackson, D. D. (1971). Thermodynamics of Gaseous Hydroxides, UCRL-51137.

JANAF (1974). Joint Army, Navy, Air Force Thermochemical Tables, 2nd ed., NSRDS-NBS 37, U.S. Government Printing Office, Washington, DC. See also later supplements for 1971-1982.

Kantrowitz, A. and Grey, J. (1951). Rev. Sci. Instru. 22, 329.

Meschi, D. J., Chupka, W. A., and Berkowitz, J. (1960). J. Chem. Phys. 33, 530.

Odoj, R., Hilpert, K., and Gerads, H. (1979). "Investigations of the Volatility of Cesium from Aluminosilicates by Mass Spectroscopy," in Scientific Basis for Nuclear Waste Management, 1, 227, G. J. McCarthy, Ed., Plenum Publishing Co., New York.

Plante, E. R. (1979). "Vapor Pressure Measurements of Potassium over K_2O-SiO_2 Solutions by a Knudsen Effusion Mass Spectrometric Method," in Characterization of High Temperature Vapors and Gases, Hastie, J. W., ed. NBS-SP 561, p. 265, U.S. Government Printing Office.

Schäfer, H., Tebben, A., and Gerhardt, W. (1963). Zeit. Anorg. Allg. Chem., 321, 42.

Skudlarski, K., Drowart, J., Exsteen, G., and Auwera-Mahieu, A. Vander. (1967). Trans. Faraday Soc. 63, 1146.

Soper, P. D. (1982). Private communication.

Wenzel, J. T. and Sanders, D. M. (1982). Phys. Chem. Glass. 23, 47.

Wicks, C. E., and Block, F. E. (1963). Thermodynamic Properties of 65 Elements and Their Oxides, Halides, Carbides, and Nitrides, U.S. Bur. Mines, Bull. 605.

8. Figure Captions

1. Schematic of vacuum enclosure and KMS mass spectrometric system.

2. Schematic of furnace and Knudsen cell.

3. Typical mass spectrum for SNW glass vapor at 1000 °C.

4. Ionization efficiency curves for Li^+, Na^+, and Ar^+ reference.

5. $P(NaBO_2)$ vs $10^4/T(K)$ for SNW glass vapor, series I data, compared with $P^o(NaBO_2)$ from JANAF [1971].

6. $P(LiBO_2)$ and $P(CsBO_2$ vs $10^4/T(K)$ for SNW glass vapor, series I data. Least squares line for $LiBO_2$ is based on runs 1 through 4 omitting two lowest temperature points from run 1. Curve through $CsBO_2$ data is based on four low temperature points from run 4. The $P^o(LiBO_2)$ reference pressure curve is from JANAF [1971]; $P^o(CsBO_2)$ is from Gurvich and Veits (1983).

7. Oxygen pressure vs $10^4/T(K)$ for SNW glass vapor, series I, run 1-5 data; the five lowest temperature points were rejected in the least squares analysis. Comparison curve is pressure for $Fe_2O_3(c) \rightarrow Fe_3O_4(c)$ from JANAF [1971].

8. Pressure of $NaBO_2$ vs $10^4/T(K)$ for SNW glass vapor, series II data. Line is least squares line from series I data (see fig. 5).

9. Pressure of $LiBO_2$ vs $10^4/T(K)$ for SNW glass vapor, series II compared with least squares line from series I data (see fig. 6).

10. Pressure of $CsBO_2$ and O_2 vs $10^4/T(K)$ for SNW glass vapor from series II data compared with least squares curve from series I data (for $CsBO_2$). Dashed curve is considered the best compromise between series I and II data for pressure of $CsBO_2$.

11. Isothermal (1265 K) dependence of log I^+_{43} ($H^{10}BO_2^+$) vs 1/2 log I^+_{18} (H_2O^+) showing expected stoichiometric behavior for the equilibrated reaction

$$1/2\ B_2O_3(\ell) + 1/2\ H_2O(g) = HBO_2(g).$$

12. Equilibrium constant vs $10^4/T(K)$ for B_2O_3-H_2O reaction shown as compared with JANAF [1971] curve.

13. Detailed schematic of assembled transpiration mass spectrometer, drawn approximately to scale.

14. Transpiration mass spectrometer inlet system showing internal details and relative location of components--<u>not</u> to scale.

15. Detailed schematic of integral capillary nozzle section of transpiration inlet system. Relative locations are given approximately to scale, except the nozzle channel, which has been enlarged for clarity. A typical experimental temperature profile along the axis of the system, obtained without the boat present, is also shown.

16. Variation of ion current ratios with temperature and time (increasing temperature run chronology). For sodium borate, I_{23}^{+}/I_{66}^{+} and for lithium borate, I_{7}^{+}/I_{50}^{+} are indicated, respectively.

17. TMS partial pressure data for metaborate and alkali species over SNW glass, with pure N_2 carrier gas at ~ 0.3 atm total pressure and a flow rate of 6 sccm. $LiBO_2$ data have been multiplied by a factor of 10 for clarity. The lines labeled Na_2CO_3 and Na_2O are for the Na decomposition pressures of these components in the SNW glass (see text).

18. Noncondensible gases observed in pure N_2 SNW glass experiments. The solid curves indicate the time as well as temperature history. Note that the curves marked CO_2 and O_2 follow the suggested Na from Na_2CO_3 curve from figure 17, whereas H_2O appears to result from a process more representative of the bulk glass. At the higher temperatures, possible formation of 44 amu HBO_2 may interfere with the CO_2 signal.

19. Comparison of metaborate partial pressure data selected from KMS and TMS experiments The solid curves shown are least squares fits to the entire ensemble of data with equal weighting, except for the $CsBO_2$ data where the first five KMS and four TMS points were selected as most representative of this species. KMS $CsBO_2$ data is from Series I multiplied by factor of two for an average of series I and II. Least squares analysis of the TMS + KMS metaborate data yields:

$$\log P(\text{atm})\ \{LiBO_2\} = (4.73 \pm 0.2) - (1.292 \pm 0.02) \times 10^4/T$$

$$\log P(\text{atm})\ \{NaBO_2\} = (4.09 \pm 0.2) - (1.190 \pm 0.02) \times 10^4/T$$

$$\log P(\text{atm})\ \{CsBO_2\} = (3.45 \pm 0.3) - (1.288 \pm 0.04) \times 10^4/T\ .$$

20. Comparison of experimental metaborate pressures with thermodynamic estimates for the major volatile Re, Ru, and Sr species. Calculations assume an oxygen partial pressure of 0.02 atm. The nominal glass composition was used with activities set equal to oxide component mole fractions.

21. Predicted metal hydroxide partial pressures, calculated for the reactions shown. Selected best thermodynamic functions have been used, with the assumption that activity equals mole fraction (or actual activity from experiment in borate cases). The interdependency between species has been approximated by assuming $P(HBO_2) = P(LiBO_2)$ for all reactions involving HBO_2, with that value set from the LiOH pressure line. Similarly, P(NaOH) was set by the reaction

$$NaBO_2 \text{ (solution)} + H_2O = NaOH + HBO_2.$$

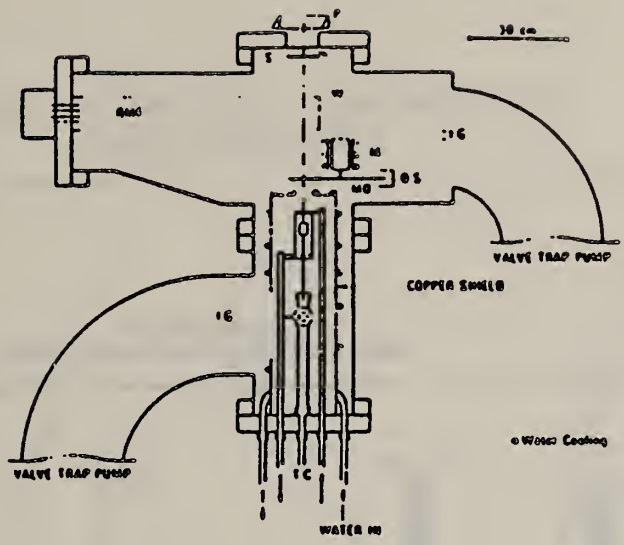

Figure 1.

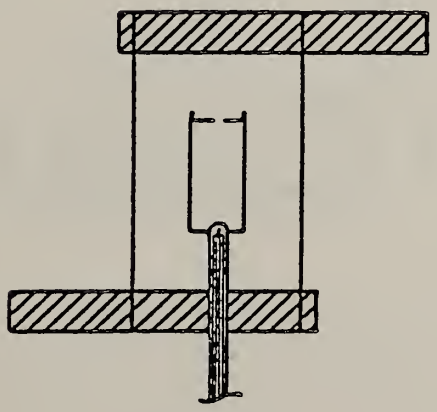

Figure 2.

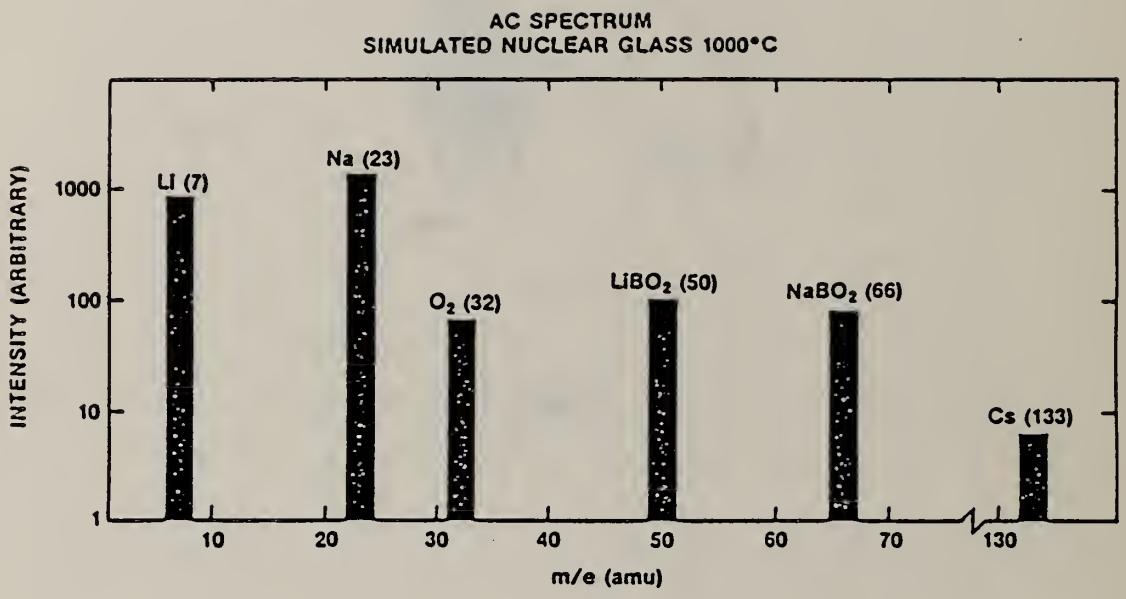
AC SPECTRUM
SIMULATED NUCLEAR GLASS 1000°C
INTENSITY (ARBITRARY)
1000
100
10
1
Li (7)
Na (23)
O2 (32)
LiBO2 (50)
NaBO2 (66)
Cs (133)
10
20
30
40
50
60
70
130
m/e (amu)

Figure 3.

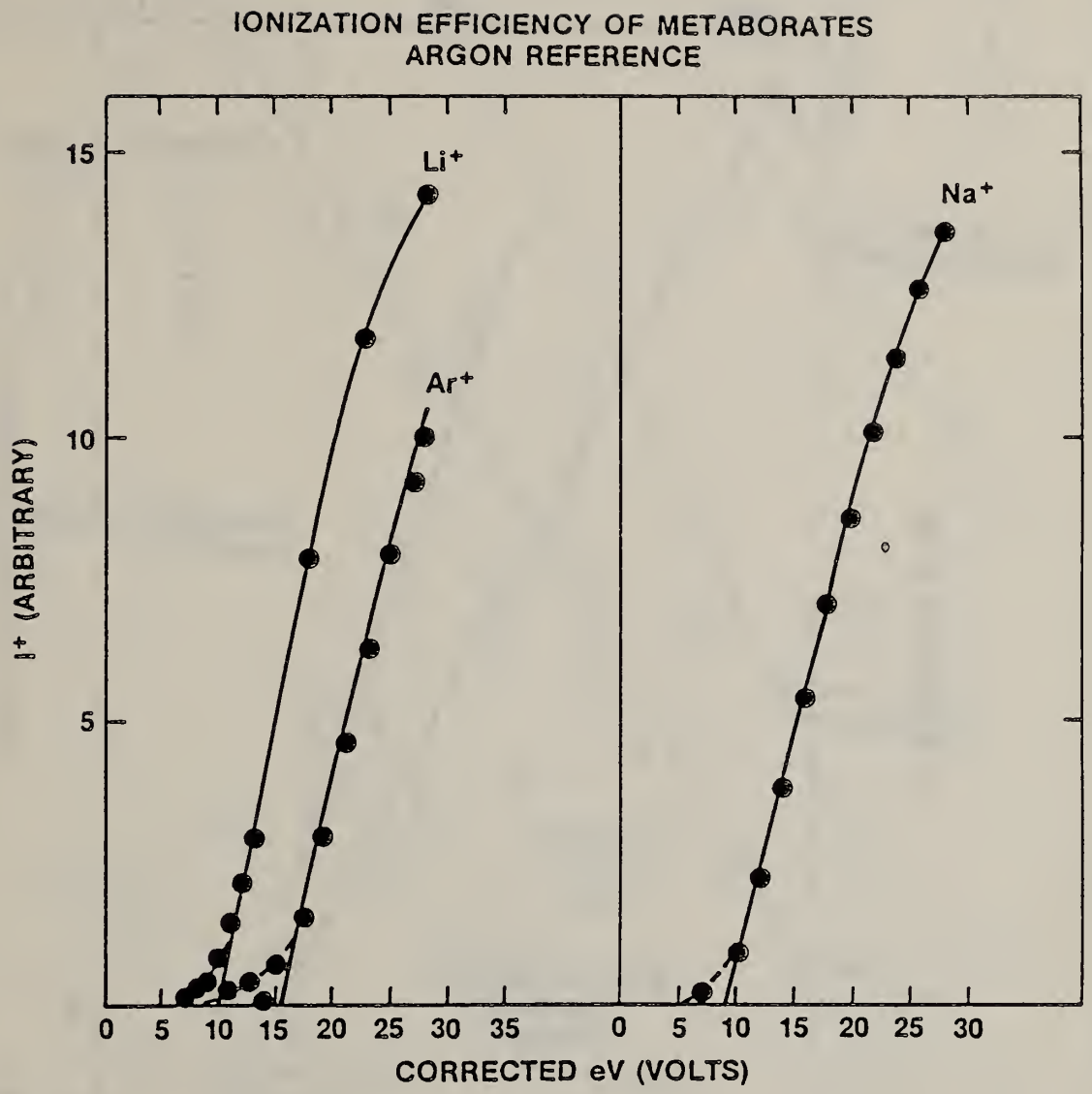
IONIZATION EFFICIENCY OF METABORATES
ARGON REFERENCE
15
10
5
I+ (ARBITRARY)
Li+
Ar+
Na+
0 5 10 15 20 25 30 35
0 5 10 15 20 25 30
CORRECTED eV (VOLTS)

Figure 4.

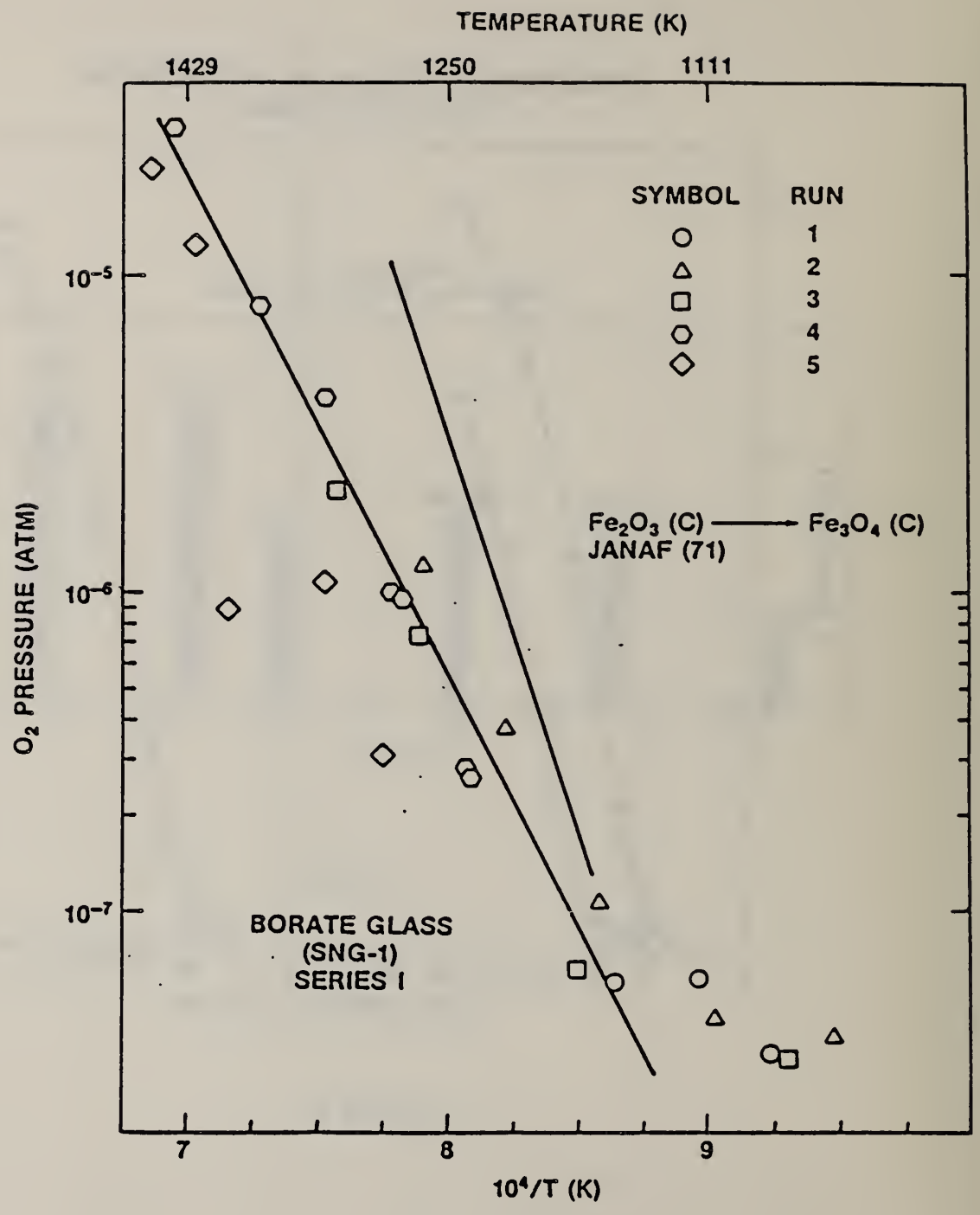
TEMPERATURE (K)
1429
1250
1111
SYMBOL
RUN
1
2
3
4
5
10^{-5}
10^{-6}
10^{-7}
O_2 PRESSURE (ATM)
Fe_2O_3 (C) ⟶ Fe_3O_4 (C)
JANAF (71)
BORATE GLASS
(SNG-1)
SERIES I
7
8
9
10^4/T (K)

Figure 5.

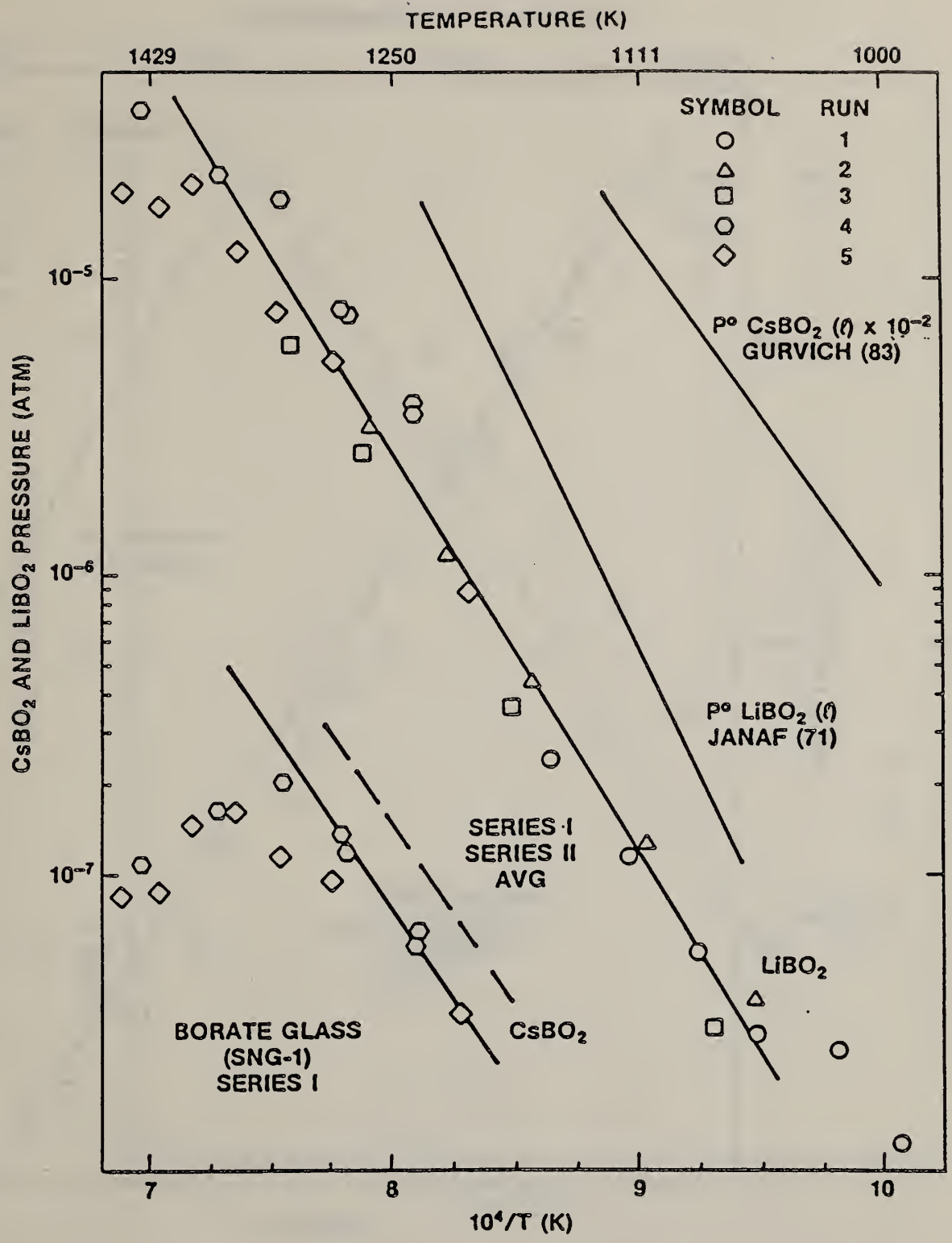
TEMPERATURE (K)
1429
1250
1111
1000
SYMBOL
RUN
1
2
3
4
5
P° CsBO2 (ℓ) x 10-2
GURVICH (83)
P° LiBO2 (ℓ)
JANAF (71)
SERIES I
SERIES II
AVG
LiBO2
CsBO2
BORATE GLASS
(SNG-1)
SERIES I
CsBO2 AND LiBO2 PRESSURE (ATM)
10-5
10-6
10-7
7
8
9
10
10⁴/T (K)

Figure 6.

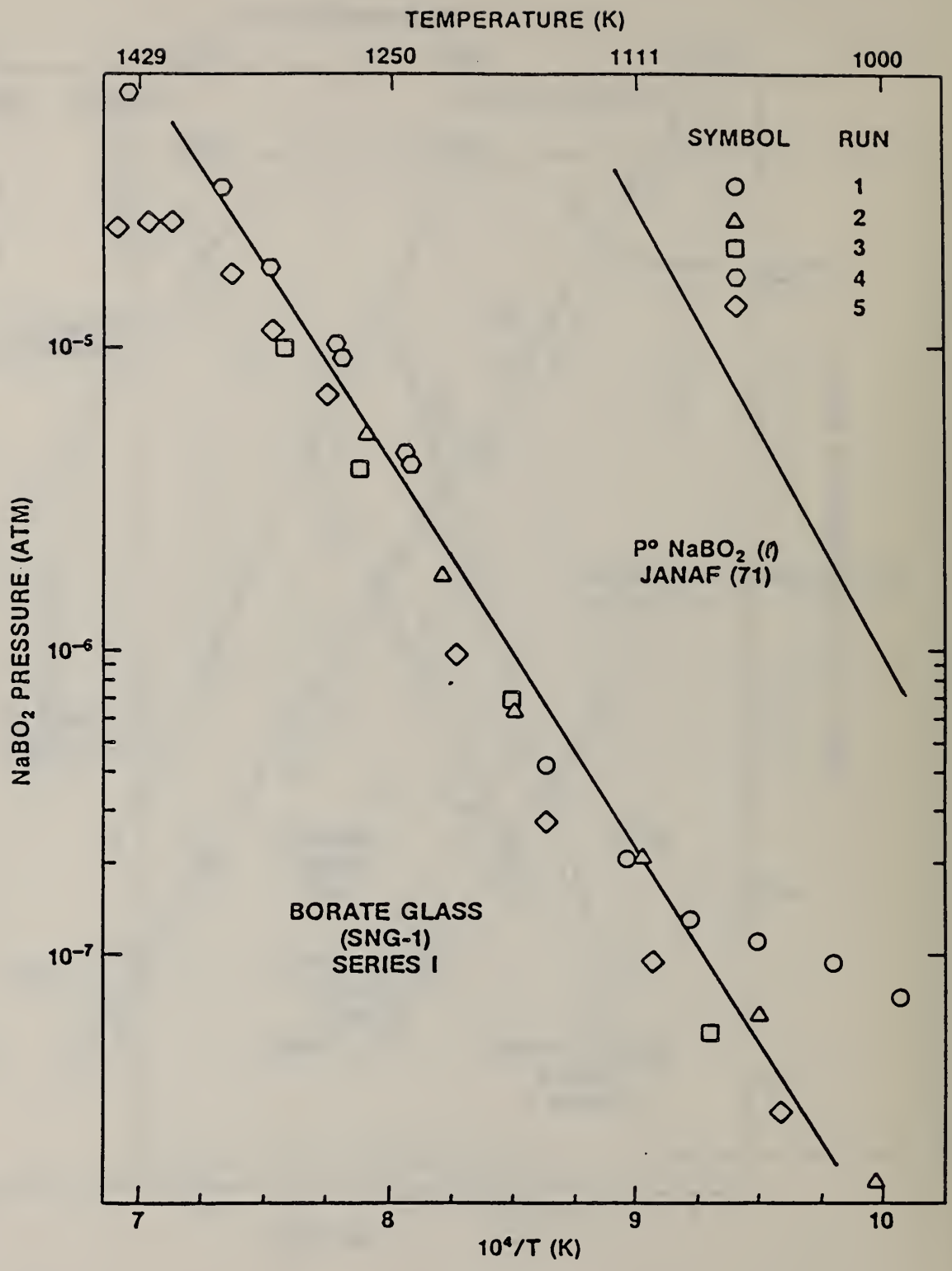
TEMPERATURE (K)
1429
1250
1111
1000
SYMBOL
RUN
1
2
3
4
5
P° NaBO2 (l)
JANAF (71)
BORATE GLASS
(SNG-1)
SERIES I
NaBO2 PRESSURE (ATM)
10-5
10-6
10-7
7
8
9
10
10⁴/T (K)

Figure 7.

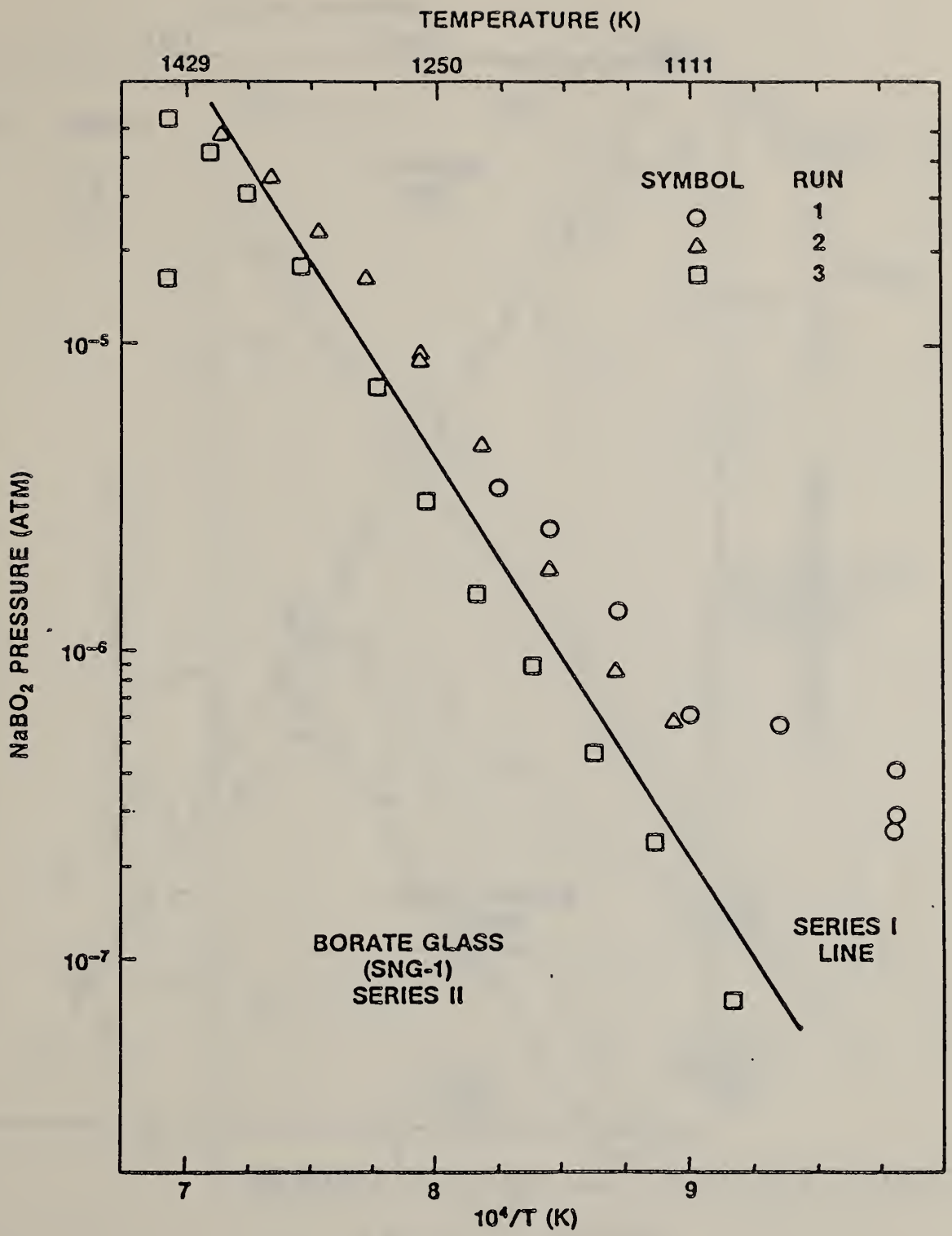
TEMPERATURE (K)
1429
1250
1111
SYMBOL
RUN
1
2
3
10^{-5}
10^{-6}
10^{-7}
$NaBO_2$ PRESSURE (ATM)
BORATE GLASS
(SNG-1)
SERIES II
SERIES I
LINE
7
8
9
$10^4/T$ (K)

Figure 8.

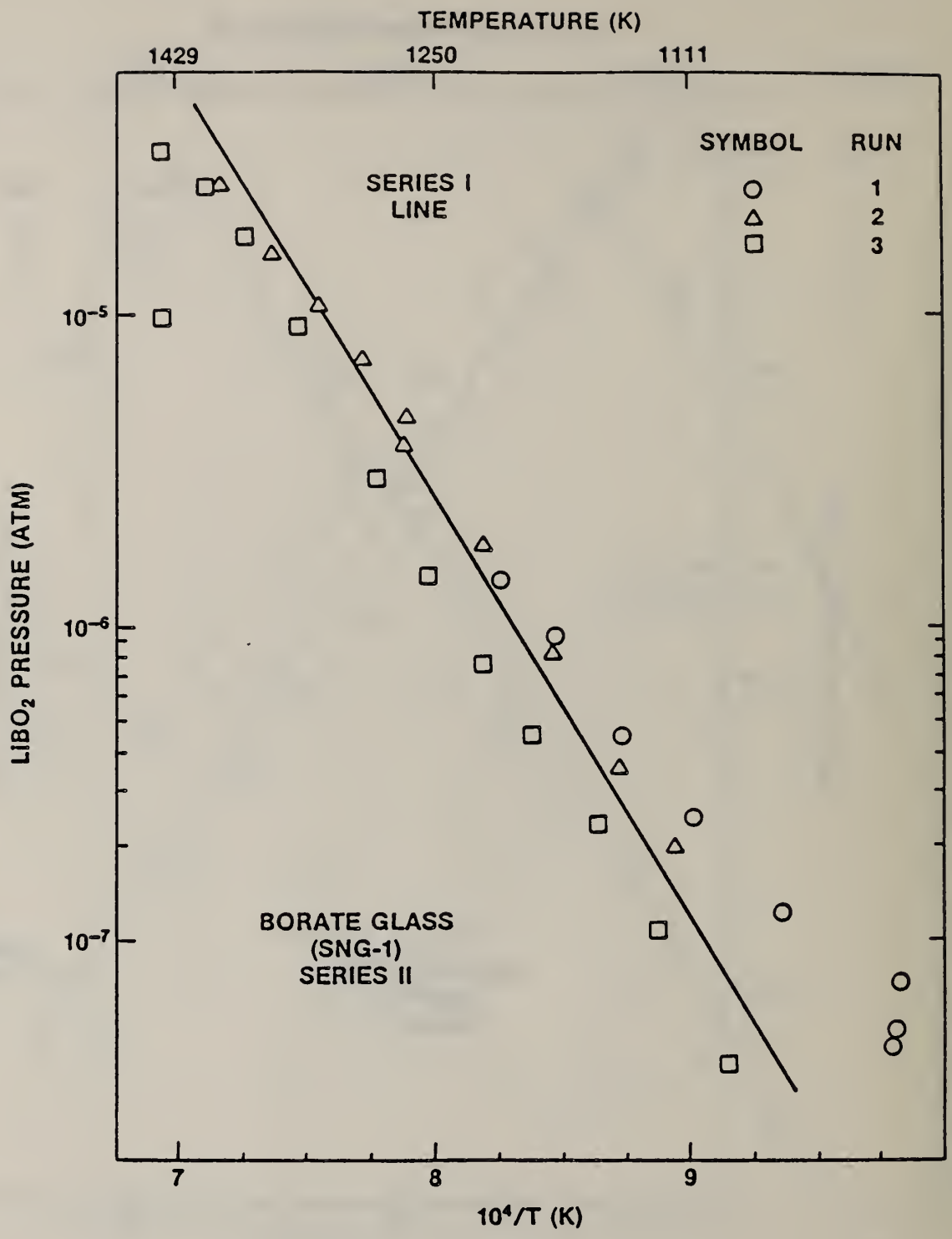
TEMPERATURE (K)
1429
1250
1111
SYMBOL
RUN
SERIES I
LINE
1
2
3
10^{-5}
10^{-6}
10^{-7}
$LiBO_2$ PRESSURE (ATM)
BORATE GLASS
(SNG-1)
SERIES II
7
8
9
$10^4/T$ (K)

Figure 9.

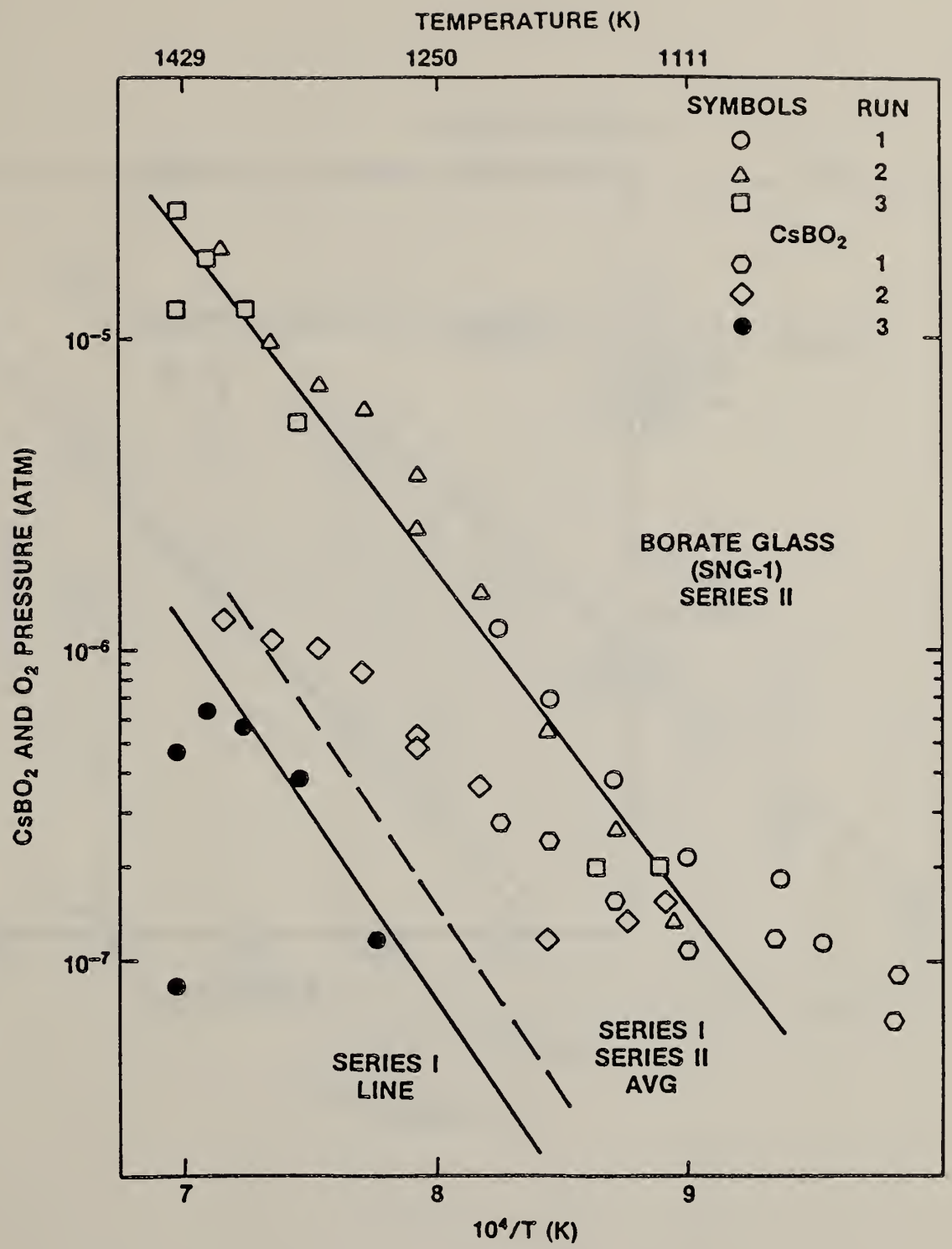
TEMPERATURE (K)
1429
1250
1111
SYMBOLS
RUN
1
2
3
CsBO2
1
2
3
BORATE GLASS
(SNG-1)
SERIES II
SERIES I
LINE
SERIES I
SERIES II
AVG
CsBO2 AND O2 PRESSURE (ATM)
10-5
10-6
10-7
7
8
9
10⁴/T (K)

Figure 10.

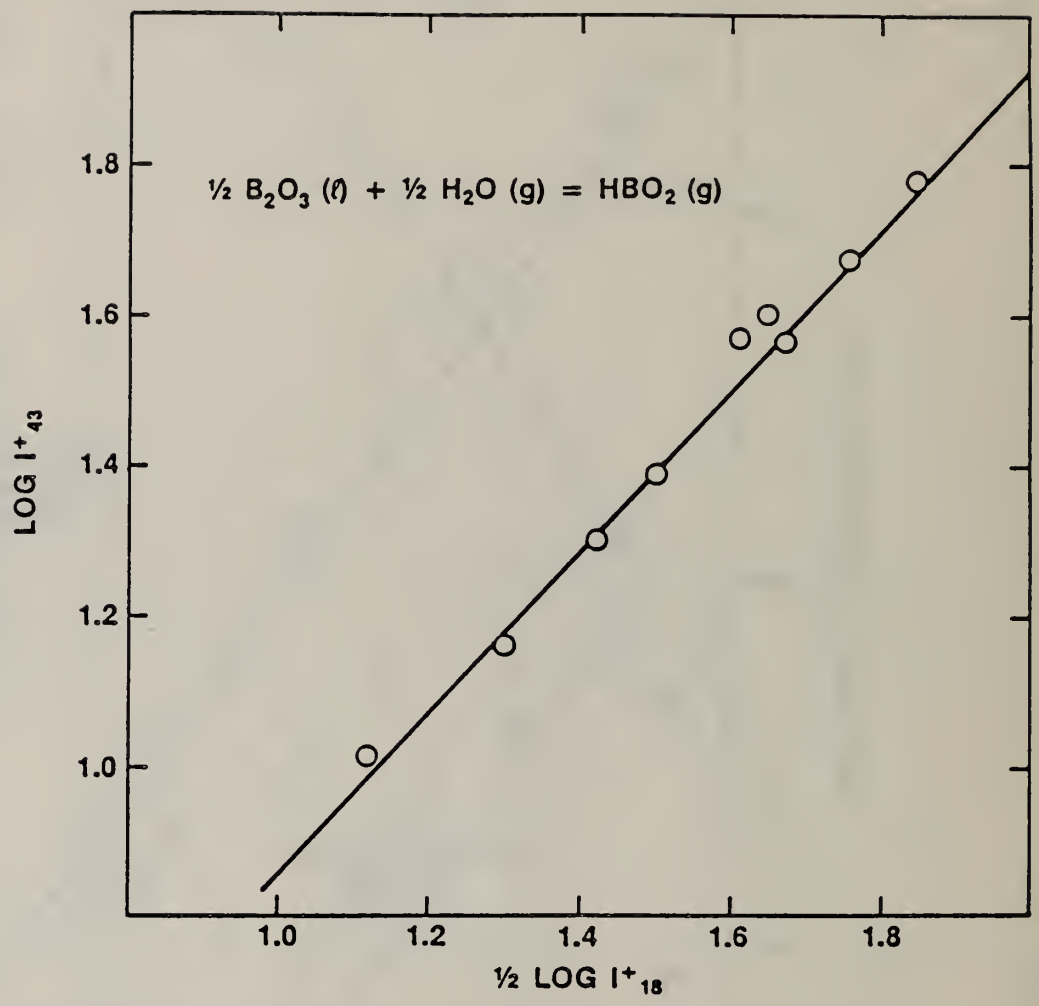

Figure 11.

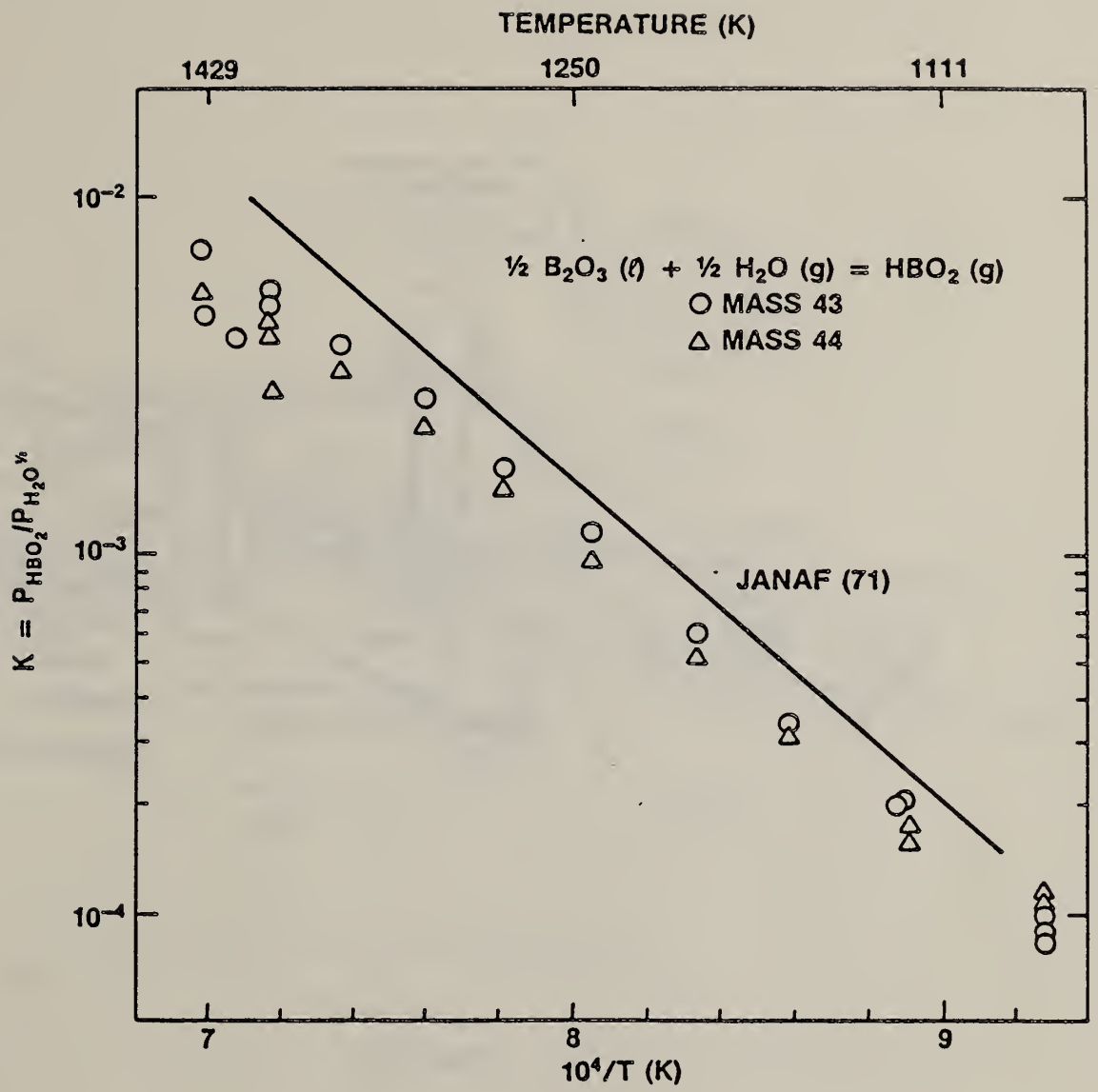
TEMPERATURE (K)
1429
1250
1111
10^{-2}
10^{-3}
10^{-4}
$K = P_{HBO_2}/P_{H_2O}^{1/2}$
½ B_2O_3 (ℓ) + ½ H_2O (g) = HBO_2 (g)
O MASS 43
Δ MASS 44
JANAF (71)
7
8
9
$10^4/T$ (K)

Figure 12.

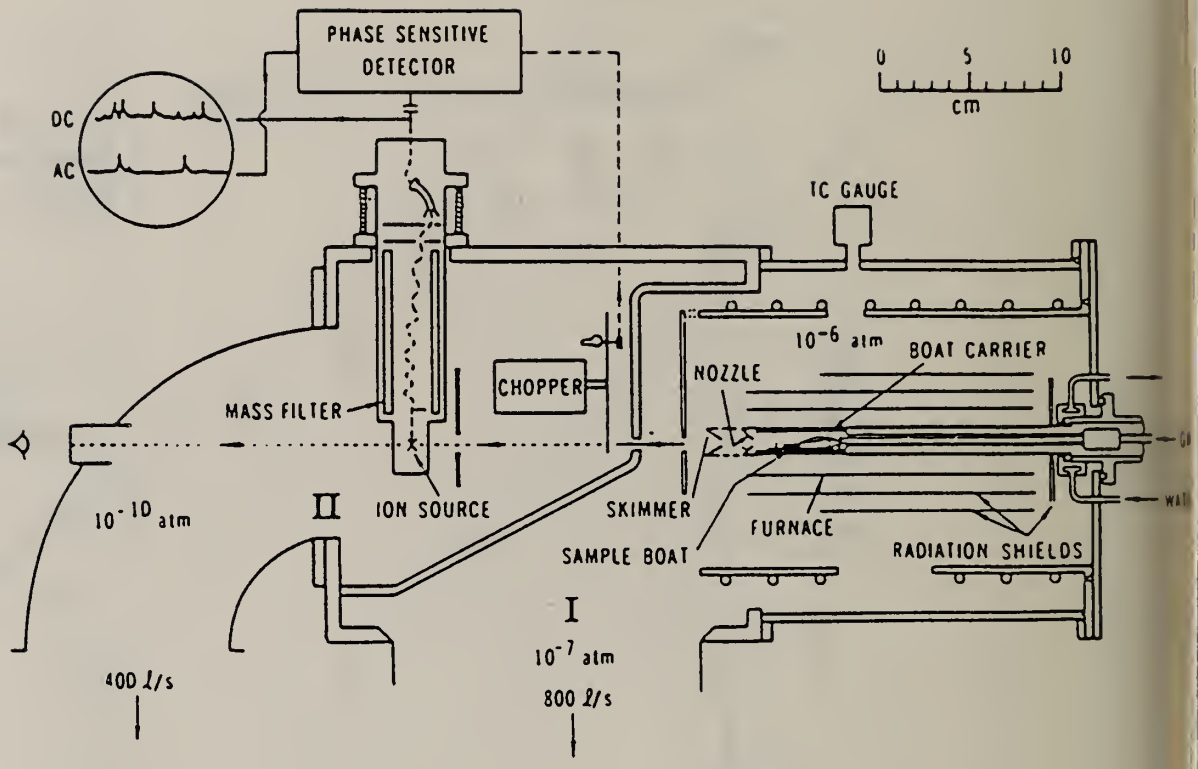
PHASE SENSITIVE
DETECTOR
DC
AC
0
5
10
cm
TC GAUGE
10^{-6} atm
BOAT CARRIER
NOZZLE
CHOPPER
MASS FILTER
10^{-10} atm
II
ION SOURCE
SKIMMER
FURNACE
SAMPLE BOAT
RADIATION SHIELDS
I
10^{-7} atm
400 l/s
800 l/s

Figure 13.

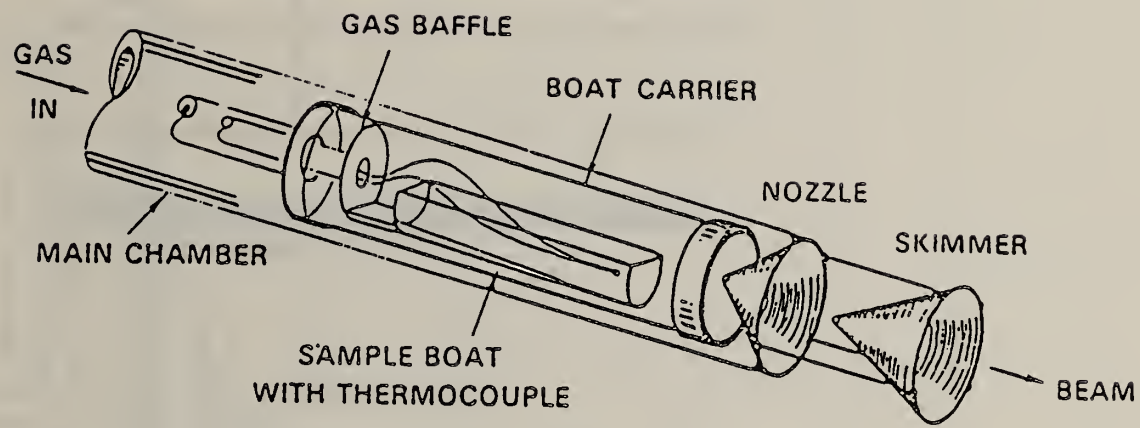
GAS
IN
GAS BAFFLE
BOAT CARRIER
NOZZLE
SKIMMER
MAIN CHAMBER
SAMPLE BOAT
WITH THERMOCOUPLE
BEAM

Figure 14.

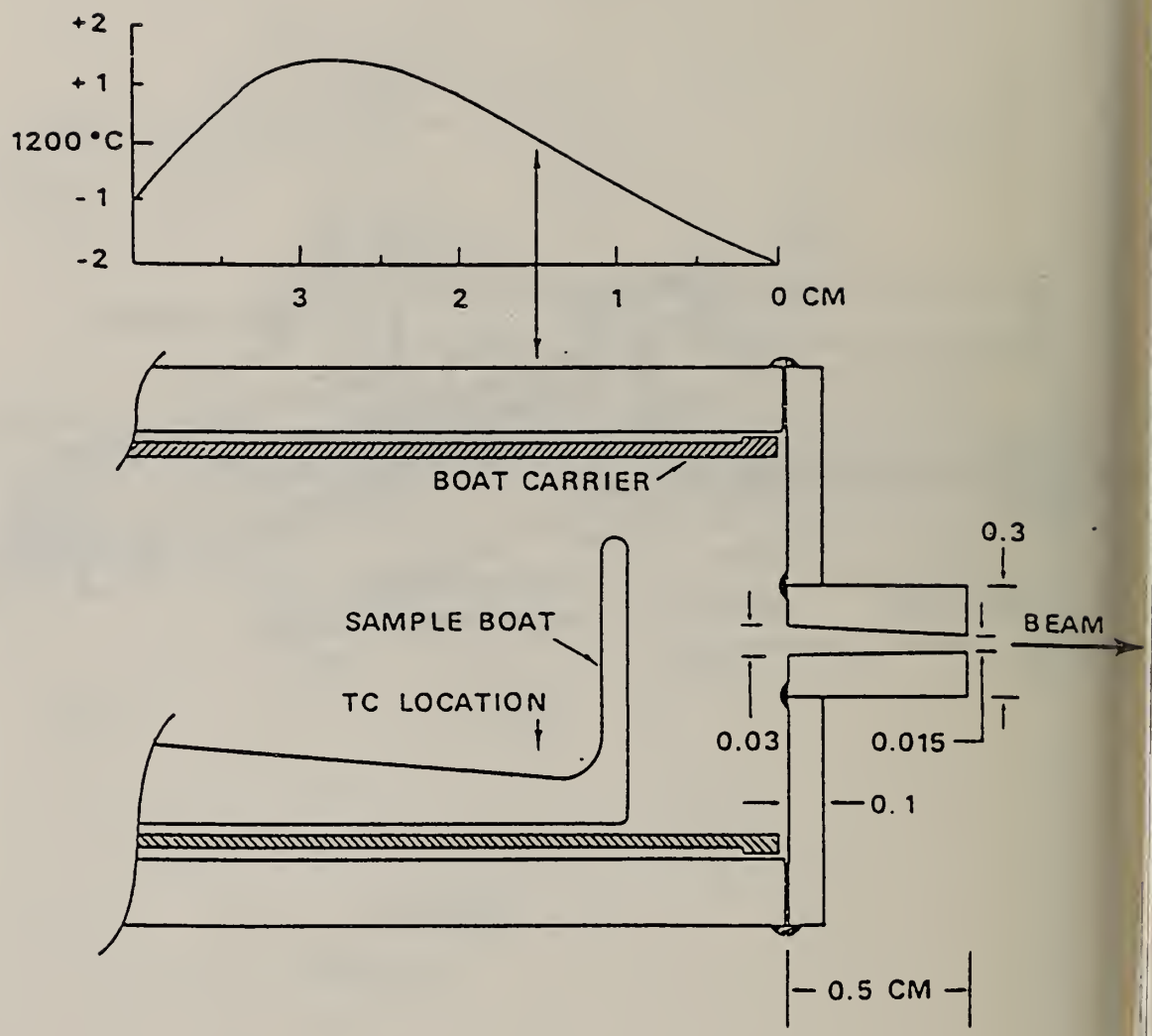
+2
+1
1200 °C
-1
-2
3
2
1
0 CM
BOAT CARRIER
SAMPLE BOAT
TC LOCATION
0.3
BEAM
0.03
0.015
0.1
0.5 CM

Figure 15.

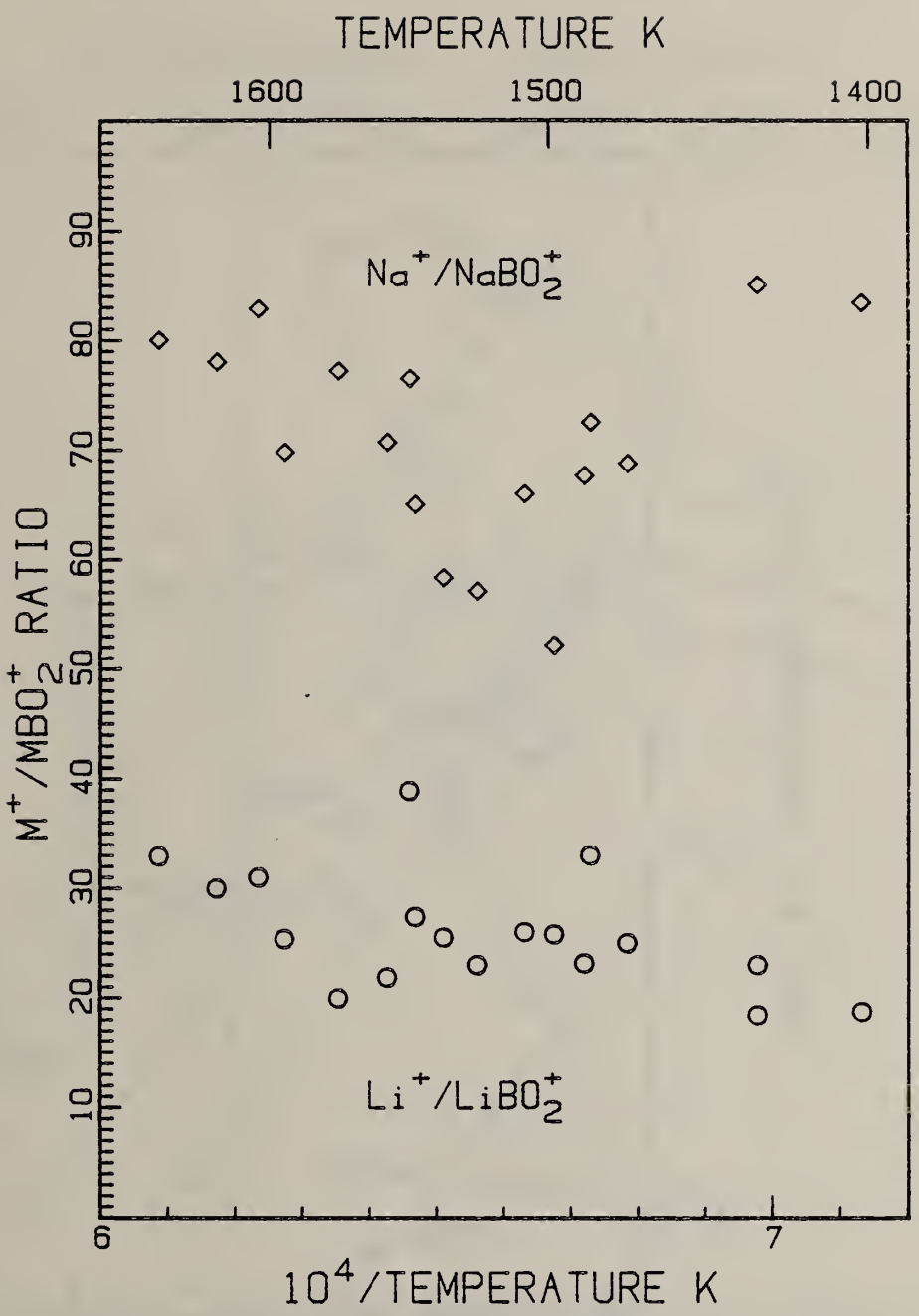
TEMPERATURE K
1600
1500
1400
$Na^+/NaBO_2^+$
$Li^+/LiBO_2^+$
M^+/MBO_2^+ RATIO
10
20
30
40
50
60
70
80
90
6
7
10^4/TEMPERATURE K

Figure 16.

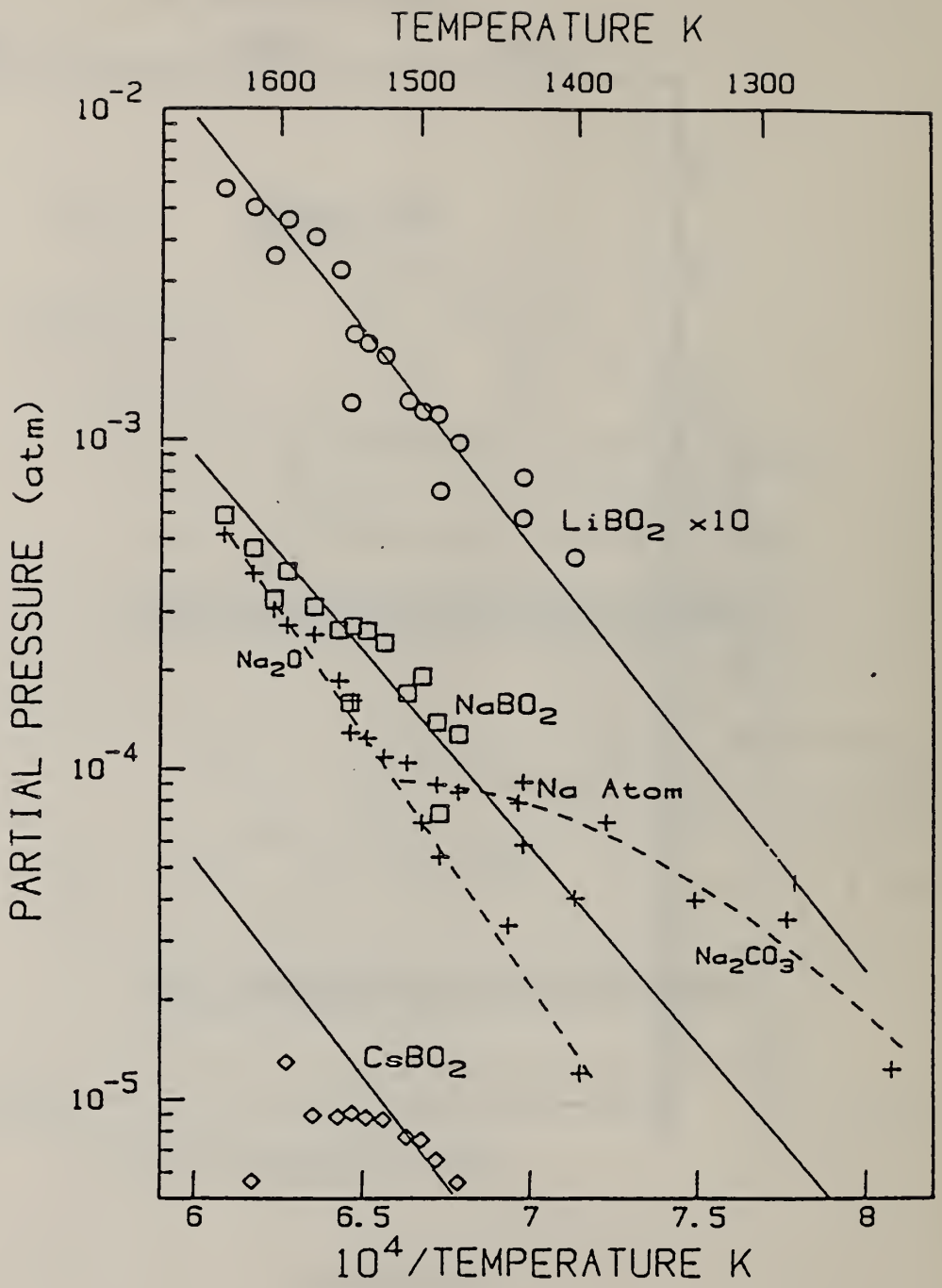
TEMPERATURE K
1600
1500
1400
1300
10^{-2}
10^{-3}
10^{-4}
10^{-5}
PARTIAL PRESSURE (atm)
$LiBO_2$ x10
Na_2O
$NaBO_2$
Na Atom
Na_2CO_3
$CsBO_2$
6
6.5
7
7.5
8
10^4/TEMPERATURE K

Figure 17.

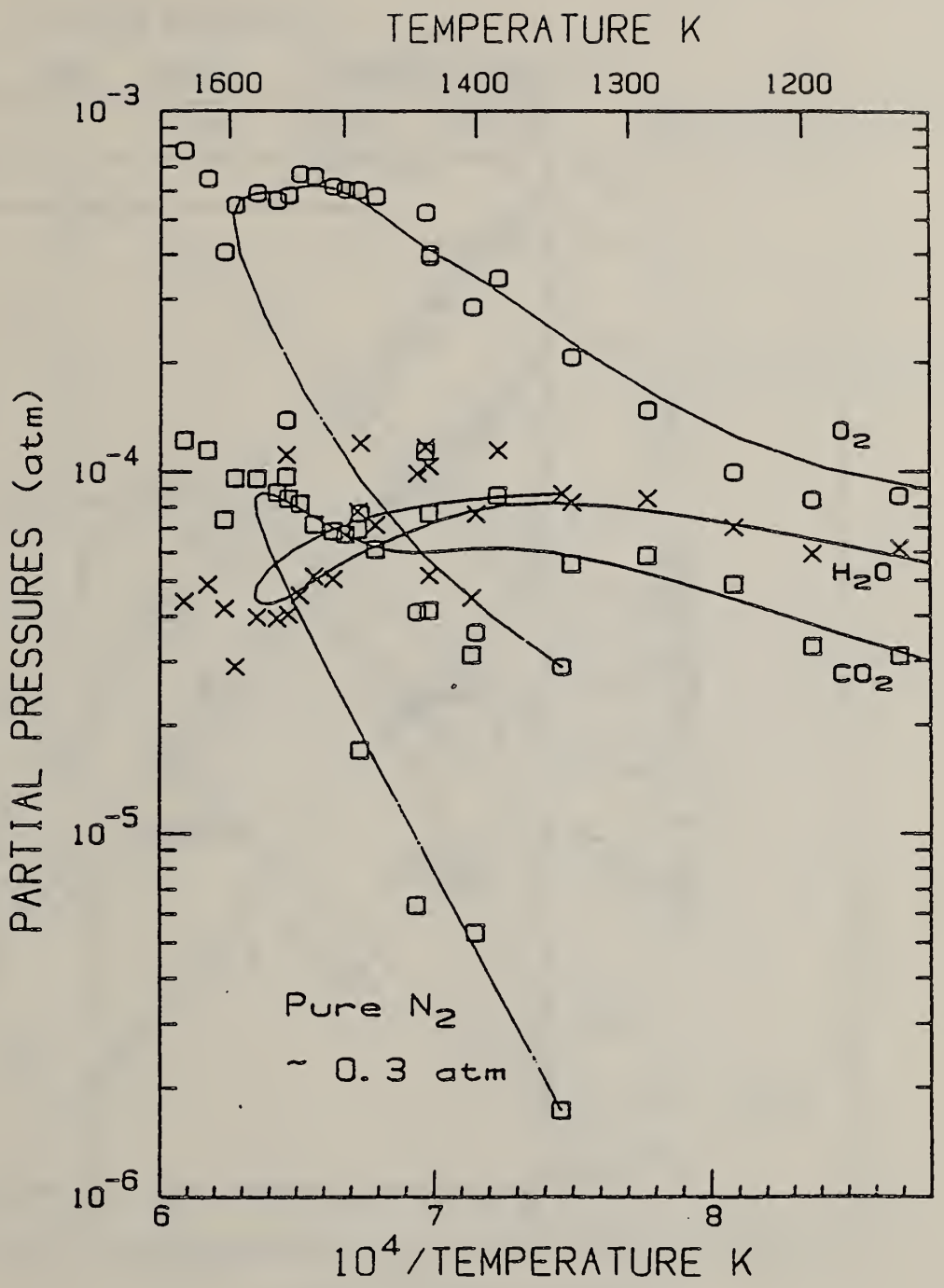
TEMPERATURE K
1600
1400
1300
1200
10^{-3}
10^{-4}
10^{-5}
10^{-6}
PARTIAL PRESSURES (atm)
O_2
H_2O
CO_2
Pure N_2
~ 0.3 atm
6
7
8
10^4/TEMPERATURE K

Figure 18.

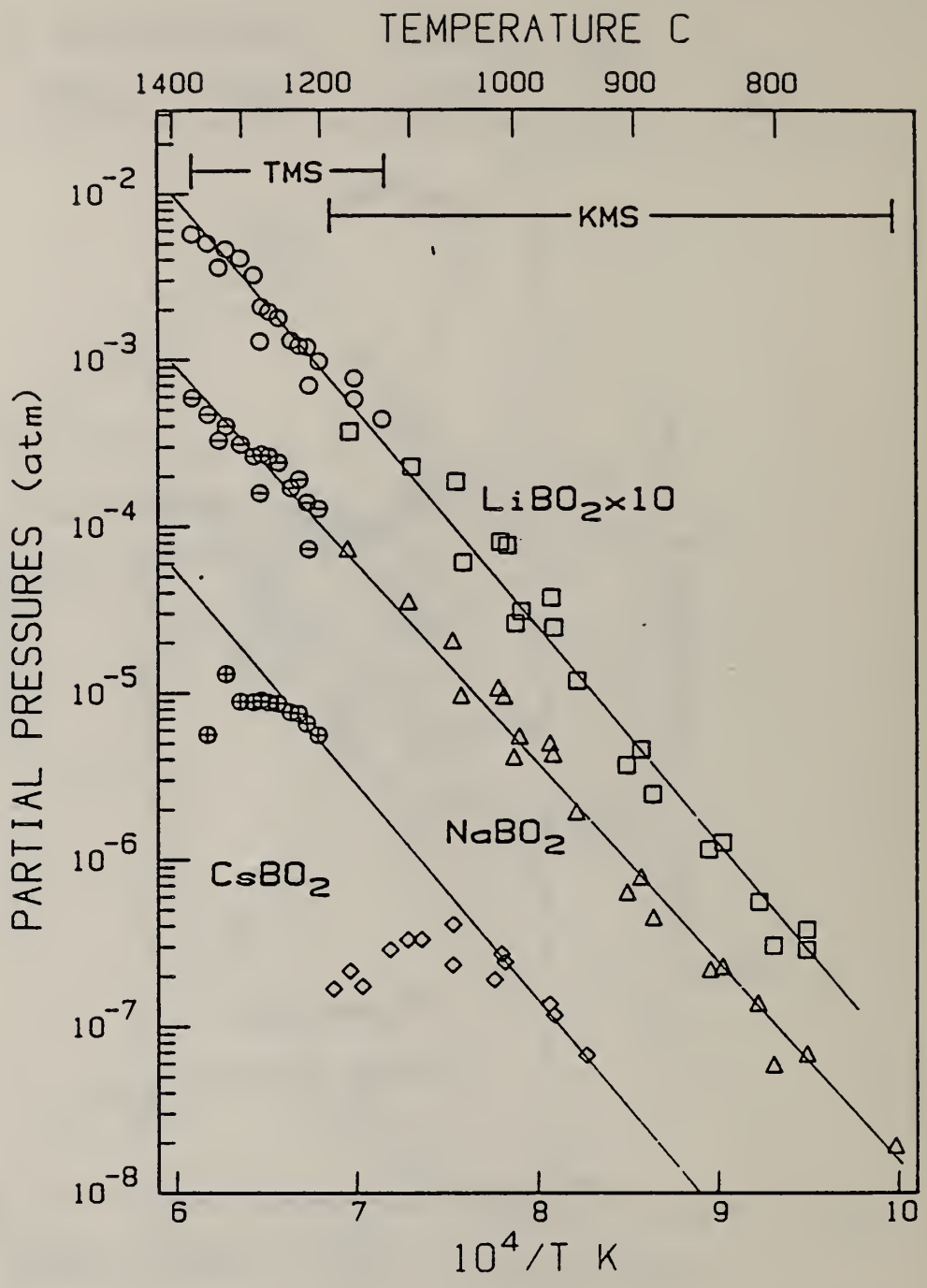
TEMPERATURE C
1400
1200
1000
900
800
TMS
KMS
10^{-2}
10^{-3}
10^{-4}
10^{-5}
10^{-6}
10^{-7}
10^{-8}
PARTIAL PRESSURES (atm)
$LiBO_2 \times 10$
$NaBO_2$
$CsBO_2$
6
7
8
9
10
$10^4/T$ K

Figure 19.

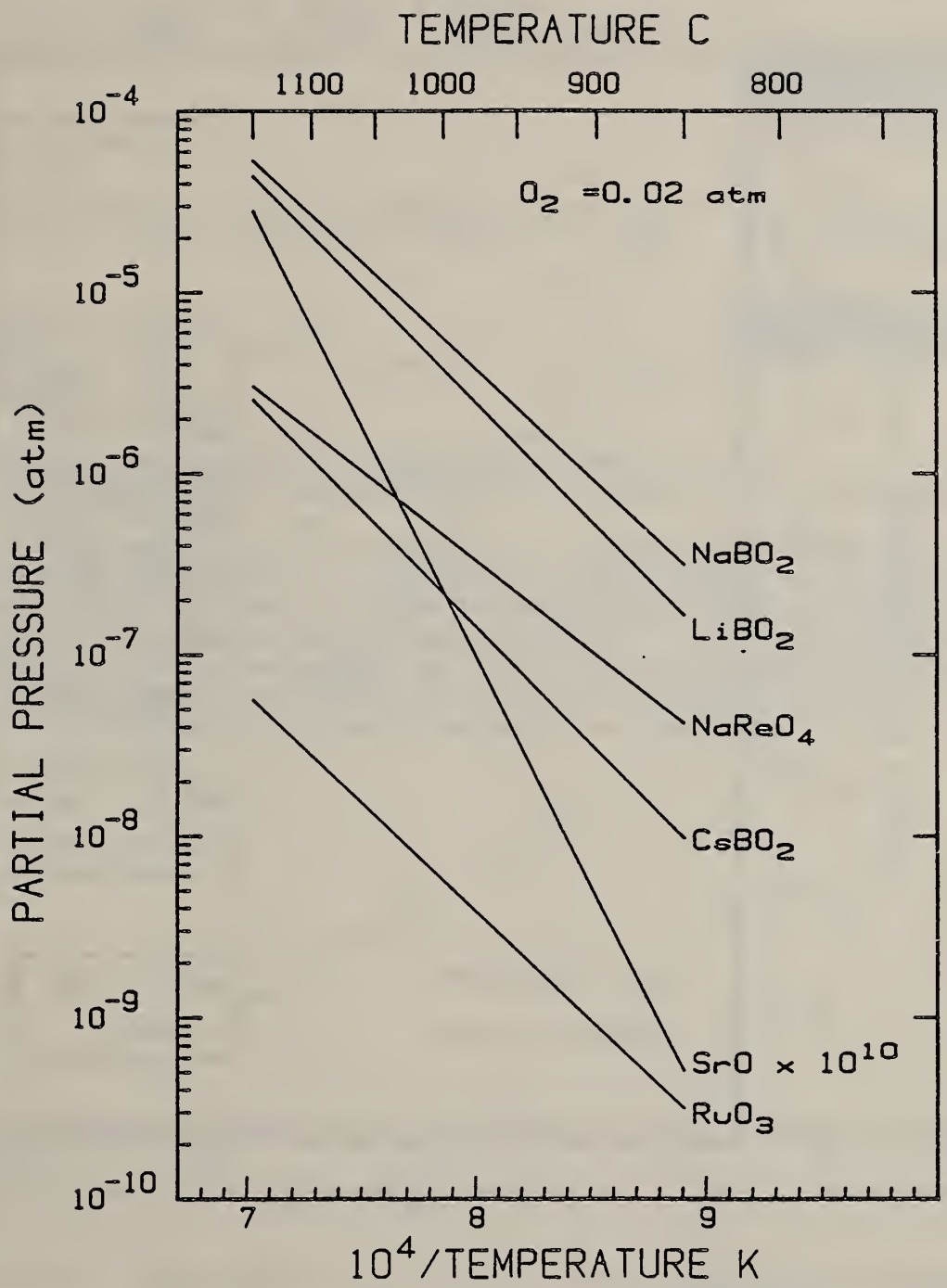
TEMPERATURE C
1100
1000
900
800
10^{-4}
10^{-5}
10^{-6}
10^{-7}
10^{-8}
10^{-9}
10^{-10}
PARTIAL PRESSURE (atm)
O_2 =0.02 atm
$NaBO_2$
$LiBO_2$
$NaReO_4$
$CsBO_2$
SrO × 10^{10}
RuO_3
7
8
9
10^4/TEMPERATURE K

Figure 20.

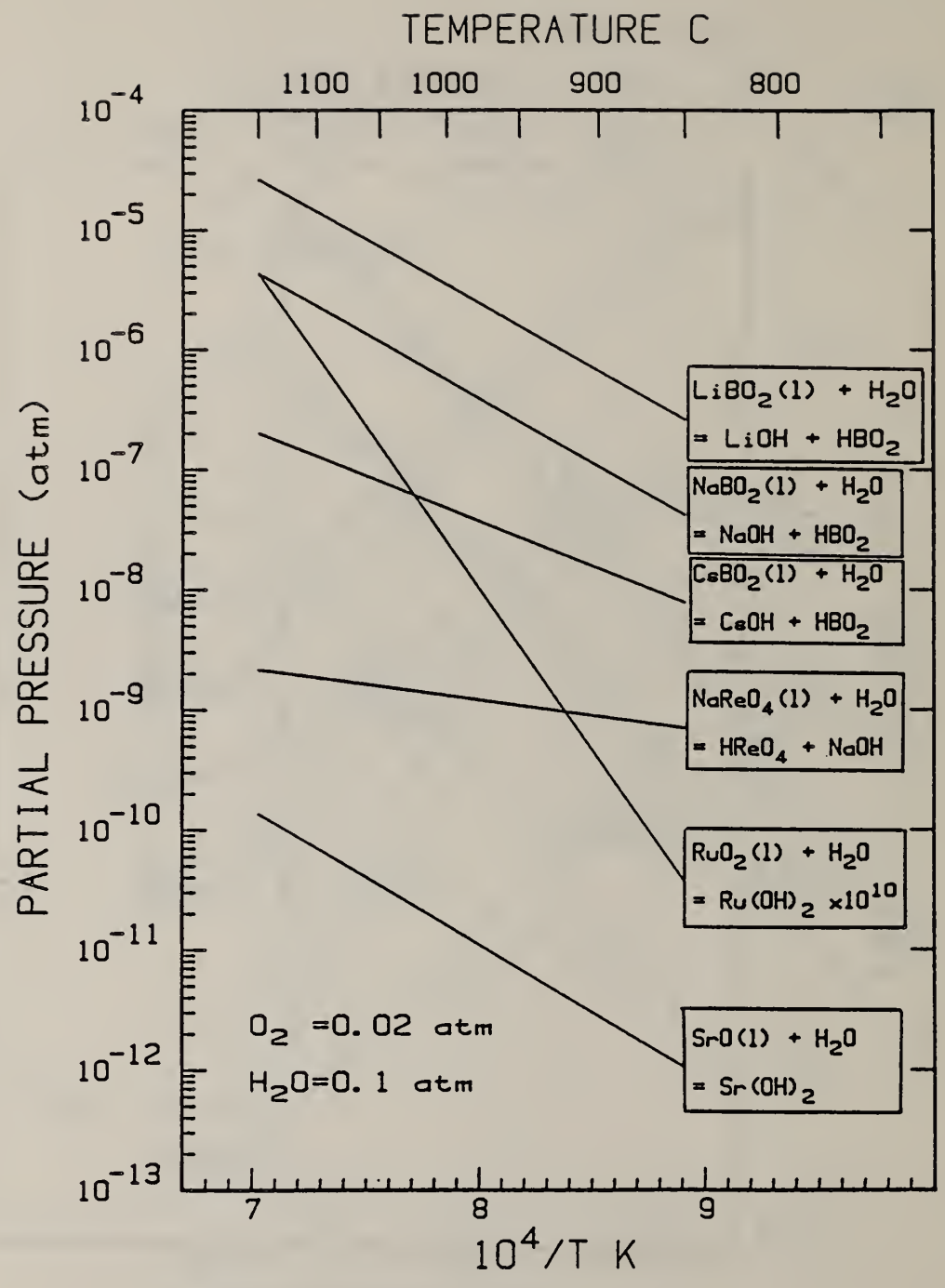
TEMPERATURE C
1100
1000
900
800
PARTIAL PRESSURE (atm)
10^{-4}
10^{-5}
10^{-6}
10^{-7}
10^{-8}
10^{-9}
10^{-10}
10^{-11}
10^{-12}
10^{-13}
$LiBO_2(l) + H_2O = LiOH + HBO_2$
$NaBO_2(l) + H_2O = NaOH + HBO_2$
$CsBO_2(l) + H_2O = CsOH + HBO_2$
$NaReO_4(l) + H_2O = HReO_4 + NaOH$
$RuO_2(l) + H_2O = Ru(OH)_2 \times 10^{10}$
$SrO(l) + H_2O = Sr(OH)_2$
O_2 =0.02 atm
H_2O=0.1 atm
7
8
9
$10^4/T$ K

Figure 21.

NBS-114A (REV. 9-78)

U.S. DEPT. OF COMM. BIBLIOGRAPHIC DATA SHEET	1. PUBLICATION OR REPORT NO. NBSIR 83-2731	2. Gov't. Accession No.	3. Recipient's Accession No.

4. TITLE AND SUBTITLE
VAPORIZATION OF SIMULATED NUCLEAR WASTE GLASS

5. Publication Date
June 1983

6. Performing Organization Code

7. AUTHOR(S)
J. W. Hastie, E. R. Plante, and D. W. Bonnell

8. Performing Organ. Report No.

9. PERFORMING ORGANIZATION NAME AND ADDRESS

NATIONAL BUREAU OF STANDARDS
DEPARTMENT OF COMMERCE
WASHINGTON, DC 20234

10. Project/Task/Work Unit No.

11. Contract/Grant No.

12. SPONSORING ORGANIZATION NAME AND COMPLETE ADDRESS *(Street, City, State, ZIP)*

13. Type of Report & Period Covered
Interim Report

14. Sponsoring Agency Code

15. SUPPLEMENTARY NOTES

☐ Document describes a computer program; SF-185, FIPS Software Summary, is attached.

16. ABSTRACT *(A 200-word or less factual summary of most significant information. If document includes a significant bibliography or literature survey, mention it here.)*

Industrial development of nuclear waste glass processing requires basic data on glass vaporization thermodynamics. Detailed mass spectrometric experiments and thermodynamic estimates have been made for vaporization of a nonradioactive borosilicate glass containing representative nuclear waste isotopes. Alkali metaborates were observed to be the dominant vapor species and their partial pressures indicate significant vapor transport under likely process conditions. The results indicate the following order of significance for vapor transport of radionuclide species, Cs ∿ Re (∿ Tc) > Ru >> Sr.

17. KEY WORDS *(six to twelve entries; alphabetical order; capitalize only the first letter of the first key word unless a proper name; separated by semicolons)*
boron; glass; nuclear waste; processing; radionuclide; silicon; thermodynamics; vaporization

18. AVAILABILITY ☒ Unlimited

☐ For Official Distribution. Do Not Release to NTIS

☐ Order From Sup. of Doc., U.S. Government Printing Office, Washington, DC 20402, SD Stock No. SN003-003-

☒ Order From National Technical Information Service (NTIS), Springfield, VA. 22161

19. SECURITY CLASS (THIS REPORT)	21. NO. OF PRINTED PAGES
UNCLASSIFIED	69
20. SECURITY CLASS (THIS PAGE)	**22. Price**
UNCLASSIFIED	$10.00

USCOMM-DC